

**Investigating a Parkinson's Associated Protein Alpha-Synuclein: A
Study of Fibril Restructuring via Lipid Binding**

by

Justin Medeiros

A Thesis

presented to

The University of Guelph

In partial fulfilment of requirements
for the degree of

Master of Science

in

Biophysics

Guelph, Ontario, Canada

© Justin Medeiros, September, 2021

ABSTRACT

INVESTIGATING A PARKINSON'S ASSOCIATED PROTEIN ALPHA-SYNUCLEIN: A STUDY OF FIBRIL RESTRUCTURING VIA LIPID BINDING

Justin Medeiros
University of Guelph, 2021

Advisors:
Vladimir Ladizhansky
Scott Ryan

Alpha-synuclein (α -syn) is a small presynaptic protein that is believed to play an important role in the pathogenesis of Parkinson's disease (PD). α -syn has been shown to cluster to presynaptic mitochondria in response to cardiolipin (CL) exposure from the inner to outer mitochondrial membrane, facilitating the restructuring of α -syn fibrils toward their non-toxic membrane-bound monomer form. We utilize solid-state Nuclear Magnetic Resonance (ssNMR) to site-specifically characterize this lipid-mediated restructuring of the fibril form. We begin with chemical shift assignments of the mobile C-terminal tail for the monomeric membrane-bound form with extension to the fibril form, then report partial assignments of the rigid fibril core. Results suggest that lipid induced restructuring is not CL specific, with similar changes to the fibril form via another anionic lipid, DOPA. Only partial transition to α -helical structure is observed while much of the original β -sheet fibril structure persists, suggesting only partial N-terminal binding.

ACKNOWLEDGEMENTS

First and foremost, I would like to thank my advisors. Thank you to Dr. Vladimir Ladizhansky for allowing me to work on the amazing NMR spectrometer which I couldn't help but stare at through the Science Complex window my very first day on campus and all during my time as a physics undergraduate student. Thank you for the NMR training and guidance. Thank you to my co-advisor Dr. Scott Ryan and member of my advisory committee, Dr. George Harauz, both for your guidance, discussions, and allowing me the pleasure of working in your labs and learning about proteins and the world of molecular and cellular biology in general. Thank you all for also giving me the chance to meet so many wonderful and intelligent people who I have learned so much from.

Thank you to those who began work on this project and to those who put in the extra effort to help train me, all of you are wonderful teachers and it was a joy to learn from you. From the current and former staff at the University of Guelph NMR Centre, to my new friends in the MCB labs, and to my fellow physics graduate students.

Thank you, Dr. Sameer Al-Abdul-Wahid, for teaching me during my initial foray into the world of NMR and for always being willing to help out, whether it be for questions regarding NMR or support with the spectrometers. Thank you also to Peter Scheffer and Dr. Andy Lo for keeping them running, and to all three of you for helping me set up and run DNP NMR, even if that work couldn't see the pages of this thesis.

Another special thank you to Dr. Vladmimir Vova Bamm for teaching me how to make alpha-synuclein and navigate work in a wet-lab, and especially for being patient with me after soaking myself with the eye washing station on my very first day. Thank you to Carla, for always being able to raise my spirits. Thank you to everyone else in the Ryan and Harauz labs, including Morgan, Brodie, Natalie, Ryan, and Evelyn for being such great sports, always willing to help me find things when I inevitably lose track of where everything is after being gone from you all for so long in between my making protein and being back with my fellow physicists.

To my fellow graduate students in the protein NMR research group as well as across the Department of Physics, you are an amazing support group and I have learned so much from you all, thank you for contributing so much to my ability to work on this project. Thanks to Jeff with help learning NMR theory and how to run the spectrometers, to Daryl for help with NMRpipe and CARRA softwares, to Xiao for always willing to teach and discuss science, and to Raoul for always being so helpful and resourceful.

Finally, thank you to all my loving family and friends. Ultimately, it is because of the endless outpouring of support I have in my life that I am able to accomplish anything. Your encouragement was never wasted, and I appreciate every single one of you. More than any, thank you to Caitlyn for being by my side throughout the entire process, and for being my biggest supporter.

TABLE OF CONTENTS

Abstract.....	ii
Acknowledgements.....	iii
Table of Contents.....	v
List of Tables.....	viii
List of Figures.....	ix
List of Abbreviations.....	xi
List of Appendices.....	xiii
1 Introduction.....	1
1.1 Parkinson's disease and α -synuclein.....	1
1.2 Structure of α -Synuclein and interactions with lipids.....	3
1.3 Investigating protein structure using NMR.....	11
2 Theory and Application of Protein Solid State Nuclear Magnetic Resonance.....	14
2.1 NMR Spectroscopy.....	14
2.2 NMR Interactions.....	17
2.2.1 Chemical Shift.....	18
2.2.2 Dipolar Coupling.....	20
2.2.3 J-Coupling.....	21
2.3 Magic Angle Spinning.....	22
2.4 Multidimensional NMR.....	27
2.5 "Mobility" filter – INEPT vs CP excitation.....	31
2.6 Characterization of Protein Structure using NMR.....	33
3 Materials and Methods.....	36

3.1	Expression and purification of α -synuclein	36
3.2	Sample preparation for NMR studies.	38
3.2.1	Preparation of fibrils.....	39
3.2.2	Liposome preparation.....	39
3.2.3	Preparation of proteoliposomes.....	40
3.3	Solid-State NMR experiments.....	40
3.3.1	^1H detected NMR experiments	41
3.3.2	^{13}C detected NMR experiments.....	44
3.4	Chemical shift assignment methods.....	45
3.4.1	Through-bond multidimensional NMR correlation methods for characterization of mobile protein fragments.	45
3.4.2	Through-space multidimensional NMR correlation methods for characterization of rigid protein fragments.	48
4	Results and Discussion.....	51
4.1	Resonance assignments of the flexible regions of monomeric α -synuclein: conformation of C-terminus in the lipid-bound and amyloid fibril states.....	52
4.1.1	Assignments and data deposition.....	52
4.2	Interaction of α -synuclein fibrils with lipids	60
4.2.1	Chemical shift assignments of α -synuclein fibrils.....	60
4.2.2	Interactions of fibrils with anionic lipids induce changes in the fibril core... 63	
4.2.3	Interactions with lipids induce mobility within otherwise structured regions along with perturbations to the C-terminus of fibrils	71
4.2.4	Discussion	73
5	Future Work	81
	References.....	84
	Appendices	95

Appendix 1: Supporting information for Chapter 4.1	96
Appendix 2: Supporting information for Chapter 4.2	99

LIST OF TABLES

Table 1.1 - List of Cryo-EM and SSNMR fibril structures and associated fibril growth conditions.	9
Table 3.1 - Summary of samples used in this study.	38

Chemical shift assignments are located in the Appendices:

Appendices 1: C-terminal tail assignments.

Appendices 2: Partial assignments of the rigid fibril core.

LIST OF FIGURES

Figure 1.1 - The three major conformations of α -synuclein.	4
Figure 1.2: Structures of published WT α -syn protofilament cores.....	10
Figure 2.1 - Magic Angle Spinning NMR experiment.	23
Figure 2.2 - ^1H decoupled ^{31}P MAS spectra of barium diethylphosphate (BDEP) with increasing ω_r	26
Figure 2.3 - Generalized scheme for a 2D NMR pulse sequences utilizing RF pulses .	28
Figure 2.4 - Multidimensional NMR spectra of (A) a 2D unresolved spectra and (B) a resolved 3D spectrum	28
Figure 2.5 - Increasing resolution via multidimensional NMR from a (A) 1D $^1\text{H}/^{13}\text{C}$ INEPT to a 2D INEPT TOBSY ^{13}C - ^{13}C correlation spectra (B).....	30
Figure 2.6 - The two 1D MAS solid-state NMR pulse sequences for excitation of (A) mobile species selectively excited using INEPT, and (B) rigid species selectively excited using CP	33
Figure 3.1 – Pulse programs for each 3D proton detection experiment	44
Figure 3.2 - (A) Schematic representation of the four experiments required for backbone chemical shift assignment of mobile protein fragments	46
Figure 3.3 - (A) Schematic representation of the three experiments required for backbone chemical shift assignment of rigid protein fragments	49
Figure 4.1 - A comparison of 2D INEPT TOBSY carbon-carbon correlation spectra . . .	54
Figure 4.2 - Backbone assignment walk using HNCA (red) and HN(CO)CA (blue) experiments for residues G132-E137 on a AS:PA100 sample.....	56
Figure 4.3 - Assignments of side chain resonances using 3D CBCAcoNH and 2D ^{13}C - ^{13}C INEPT TOBSY correlation spectra collected on AS:PA100 sample.....	57
Figure 4.4 - Secondary $^{13}\text{C}\alpha$ shifts of sequentially assigned residues in the C-terminus of α -syn bound to DOPA:DOPC LUVs	58
Figure 4.5 - A representative backbone walk for residues G86-A90	61
Figure 4.6 - Amino acid sequence of α -syn, with residues assigned shown in bold and secondary structure indicated	62

Figure 4.7 - Chemical Shift Index (CSI) for assigned residues in a-syn fibrils	62
Figure 4.8 - Overlay of 2D ^{13}C - ^{13}C CP DARR spectra.....	65
Figure 4.9 - Expanded amino acid specific regions of the 2D ^{13}C - ^{13}C CP DARR.....	66
Figure 4.10 - Overlay of 2D NCA spectra.....	68
Figure 4.11 - Overlay of 2D ^{13}C - ^{13}C INEPT TOBSY spectra	73
Figure 4.12: Cryo-EM cross-sections of fibril polymorphs	78
Figure 4.13 - A model representation of fibril refolding via excess anionic lipid interactions.....	80

LIST OF ABBREVIATIONS

α -syn	Alpha-synuclein
CD	Circular dichroism
CEST	Chemical exchange saturation transfer
CL	Cardiolipin
CSA	Chemical shift anisotropy
CP	Cross-polarization
Cryo-EM	Cryogenic electron microscopy
CSI	Chemical shift index
DLS	Dynamic light scattering
DARR	Dipolar-assisted rotational resonance
DOPA	1,2-dioleoyl-sn-glycero-3-phosphate
DOPC	1,2-dioleoyl-sn-glycero-3-phosphocholine
DREAM	Dipolar Recoupling Enhanced by Amplitude Modulation
DSS	2,2-dimethyl-2-silapentane-5-sulfonic acid
<i>E. coli</i>	<i>Escherichia coli</i>
FID	Free induction decay
IDP	Intrinsically disordered protein
INEPT	Insensitive Nuclei Enhanced by Polarization Transfer
IMM	Inner mitochondrial membrane
LB	Lewy body
LUV	Large unilamellar vesicle
NAC	Non-A β -amyloidogenic component
MAS	Magic angle spinning
MSA	Multiple system atrophy
OMM	Outer mitochondrial membrane
PA	Phosphatidic acid
PAS	Principal axis system
PD	Parkinson's disease

PLR	Protein-to-lipid molar ratio
PMCA	Protein misfolding cyclic amplification
ppm	Parts per million
PFF	Pre-formed fibrils
RF	Radio frequency
RFDR	Radio-frequency driven recoupling
SNR	Signal-to-noise ratio
ssNMR	Solid-state nuclear magnetic resonance
TOBSY	Total through-bond correlation spectroscopy
TOCL	Tetraoleoyl cardiolipin

LIST OF APPENDICES

Appendix 1: Supporting information for Chapter 4.1

Appendix 2: Supporting information for Chapter 4.2

1 Introduction

1.1 Parkinson's disease and α -synuclein

Parkinson's disease (PD) is a neurodegenerative disorder causing impaired motor function, affecting over 1% of the global population over the age of 65, classifying it as the world's most common degenerative movement disorder.¹ Common symptoms include slowed movement, rigidity and resting tremors, all attributed to a continual reduction of concentration of the neurotransmitter, dopamine.¹ This depletion directly follows the loss of dopaminergic neurons in the substantia nigra *pars compacta* portion of the midbrain and the presence of proteinaceous neuronal inclusions known as Lewy Bodies (LBs), both hallmarks of PD.^{1,2,3} Symptoms worsen given continual loss of dopaminergic neurons and spread of LB pathology across the brain, including to the hippocampus and cortex, giving rise to other LB diseases termed 'synucleopathies'. These include the onset of Lewy Body dementia, as well as in multiple system atrophy (MSA) and varying cases of Alzheimer's disease.^{3,4}

LBs are the accumulation of many misfolded proteinaceous aggregates and other cellular matter in the cell soma of neurons, a main component of which is the fibril form of α -synuclein (α -syn), a small 140-residue (14.4 kDa) protein whose aggregation into amyloidogenic fibrils characterizes synucleopathies.¹⁻⁶ The function of α -syn is not yet entirely understood, although many of its proposed activities have been noted in reference 7, and it is suggested that the protein must play a role in neurotransmitter release,^{8,9} maintenance of synaptic vesicle pools^{10,11} and modulation of synaptic plasticity.^{12,13} α -syn exists in a tightly regulated equilibrium between its monomeric

soluble and anionic-membrane bound forms, with over or under-expression of the protein disturbing this equilibrium, leading to deficiencies in synaptic transmissions.¹⁴ The importance of α -syn in PD pathology is well supported by observed mutations of the *SNCA* gene which codes for α -syn. Several missense mutations are causal in early-onset familial cases of the disease (e.g. A53T, A30P, E46K) as well as both duplication or triplication events which spur PD pathology via over-expression.^{1,4,5,15} While the early stages of LB aggregates (α -syn protofibrils) are suggested to be the most toxic form,¹ the pathway for the formation of these aggregates is not yet fully understood, although it is apparent that they can begin formation both in solution or on membrane surfaces, with *SNCA* mutations associated with early-onset disease, resulting in an increased capacity for α -syn aggregation.^{16,17}

In cells, α -syn interacts with both pre-synaptic vesicles as well as other cellular membranes. One such relevant relationship regarding PD is between α -syn and neuronal mitochondria. Notably, misfolded or oligomeric α -syn has been shown to localize to these mitochondria, contributing to their dysfunction and oxidative stress.¹⁸ Mitophagy precedes cell death resulting in the transfer of fibrils to neighboring neurons in prion-like behavior, triggering further neuronal degradation.¹⁹ Mitochondrial stresses, including the exposure to the pesticides associated with increased risk of PD onset, such as rotenone, have been shown to induce the externalization of a unique mitochondrial anionic phospholipid cardiolipin (CL) from the inner mitochondrial membrane (IMM) to the outer mitochondrial membrane (OMM).²⁰

Using circular dichroism (CD) spectroscopy, CL-containing large unilamellar vesicles (LUVs) mimicking the OMM were shown to have the capacity to bind each of the soluble wild type (WT), A53T and E46K α -syn variants and convert them into the α -helical membrane-bound conformation in a CL dependent manner, albeit with faster kinetics for the WT.¹⁹ Furthermore, CL exposure to the OMM was also shown to promote the dissolution of the β -structured fibrils comprised of the WT, A53T and E46K α -syn to a predominantly α -helical conformation, again in a CL dependent manner, suggesting significant refolding of the fibrils to their monomeric membrane-bound conformation.¹⁹ This occurs more quickly and with greater efficiency for WT fibrils than for A53T and E46K fibrils, suggesting the mutated forms have increased resistance to refolding via lipid-binding.¹⁹ This refolding effect is of utmost interest as it poses a means for fibril dissolution, calling to question the fibril-lipid interactions responsible as well as the actual conformation of the refolded state. These outstanding questions form the basis of this thesis, spurring the structural analysis of the WT protein when exposed to anionic LUVs by solid-state nuclear magnetic resonance (ssNMR).

1.2 Structure of α -Synuclein and interactions with lipids

The structure of α -syn is extremely diverse, with three separate structural conformations containing unique secondary structure elements, illustrated in **Figure 1.1**. Monomeric in both its cytosolic and membrane-bound forms (although a single study suggests the existence of helical tetramer form in solution)²¹ it alternates between an intrinsically disordered protein (IDP – random coil, lacking secondary structure) in

solution to a mostly rigid α -helical formation when lipid-bound.²² This is in contrast to its aggregated fibril form, which contains a β -sheet rich core. The protein is considered to have three structurally and functionally distinct regions across each of these conformers. The lipid interacting and positively charged N-terminus (residues 1-60), the non-A β -amyloidogenic component necessary for β -sheet aggregation (NAC domain, residues 61-95) and the consistently unstructured and mobile C-terminal tail containing acidic and proline residues facilitating interactions with over 30 proteins (residues 96-140).^{5,13,23}

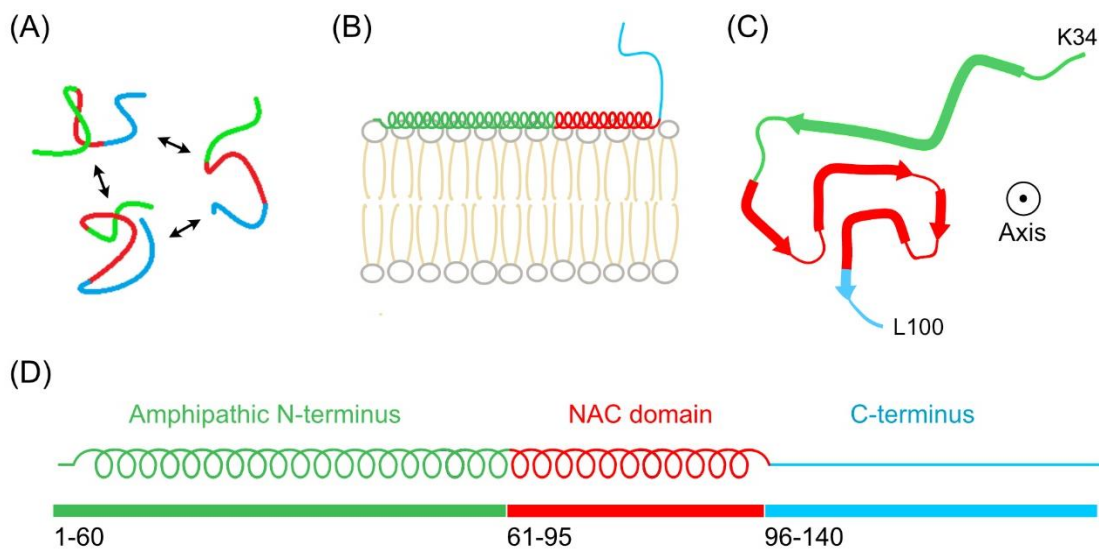


Figure 1.1 - The three major conformations of α -synuclein. (A) Unstructured cytosolic form, (B) α -helical membrane-bound form represented by the elongated shape, and (C) cross sectional view of the fibril form (structure adapted from PDB 2N0A, a nuclear magnetic resonance

determined structure of α -syn fibrils)²⁴. (D) All structures are colour coded based on the three aforementioned domains: N-terminus (green), NAC domain (red), and C-terminus (blue).

Lipid-bound α -syn binds specifically to the surface of anionic membranes, exhibiting largely α -helical structure, while also able to bind to SDS detergent micelles.^{5,25,26,27} Phospholipid vesicle bound α -syn exhibits either a broken or single rigid α -helix either partially or fully extending from the N-terminus up to the beginning of the flexible C-terminal tail at residue 96, containing 7 imperfect KTKEGV repeat motifs.^{26,28} SDS micelle-bound α -syn exhibits an interrupted α -helix via a several residue long loop, doubling back on itself in an anti-parallel fashion, conforming to the sharper curvature of the micellar surface and potentially suggesting curvature to play a major role in the binding mode of α -syn.^{5,26,27} Interactions with lipids were shown to be stabilized by both electrostatic and hydrophobic interactions of the amphipathic helix with anionic lipid headgroups and internal non-polar tails.²⁶ The N-terminus embeds itself within the membrane surface, with its positively charged residues oriented sideways to interact strongly with the negatively charged lipid headgroups.²⁶ The inside facing non-polar residues interact with the non-polar interior of the membrane while the outward facing polar residues interact with the polar solvent, altogether acting as a rigid and thermodynamically favoured N-terminal anchor, albeit still relatively mobile given the fluidity of membrane surfaces.²⁶ Furthermore, Fusco *et al.* utilized solid-state Nuclear Magnetic Resonance (ssNMR) and solution NMR chemical exchange saturation transfer (CEST)²⁹ measurements to determine that under their synaptic vesicle-like conditions, the helical anchor is strongest from residues 1-26, whereas the

NAC region essential for fibrilization acts as a modulator for the affinity of α -syn membrane binding (residues 26-97), transiently binding to the membrane.³⁰ This aggregation prone region is therefore more likely to be structurally rigid when bound to membranes with a higher α -syn binding affinity, potentially suggesting the lipid composition of membranes to be pivotal in defining the structural nature of lipid-bound α -syn, and potentially impacting fibrillogenesis and toxicity.^{30,31} Recent studies of fibrils in the presence of lipids have shown the fibril N-terminus to anchor fibrils or smaller oligomers to membrane surfaces, facilitating penetration of the fibril core into the lipid membrane. The insertion of both the monomeric and fibrillar forms can affect membrane properties, leading to membrane disruption or permeabilization.³¹

While the exact mechanisms behind fibril formation are yet to be fully understood, aggregation can occur both in solution and on membrane surfaces. Fibrillogenesis on phospholipid vesicles begins with the binding of the helical form prior to conversion to β -sheet structure indicative of fibril formation.^{17,32} Interestingly, the presence of anionic lipids has been shown to both inhibit and induce fibril formation,^{33,34} leading to the notion that fibril formation depends naturally on the protein concentration and the protein to lipid ratio.³⁵ When over-expressed in solution, soluble α -syn can aggregate to form β -sheet plaques which initially adopt a spherical morphology from which the elongated β -sheet fibril morphology originates.¹⁷ A recent study suggested the N- and C-terminus form an unstructured and “fuzzy” like surface around these oligomers, recruiting monomeric α -syn and initiating secondary nucleation of the fibril form.³⁶

Several studies suggest α -syn fibrils act similarly to prions, inducing the formation of fibrils by recruiting non-aggregated α -syn within otherwise healthy neighboring neurons, further propagating pathology from cell to cell.³⁷ This prion-like behaviour and resulting pathology is directly linked to the fibril structure, which itself directly depends on the solution and agitation conditions in which the fibrils form.³⁸ As a result, multiple structural studies showcase a polymorphic and heterogeneous nature of the fibril form, complicating the characterization of fibril-lipid interactions.^{17,39,40,41,42,43,44,45,46} A β -structured NAC domain remains the core feature of each fibril polymorph, forming a Greek-key or three-layered L shaped motif that constitutes the fibril core. While the overall topology generally remains similar in this way, differences between polymorphs are largely based on the particular arrangement of several β -strands and turns, side-chain packing, longitudinal fibril twist, and number of protofilaments or their diameter.⁴⁷ **Table 1.1** lists each of the solved WT α -synuclein fibril structures (illustrated in **Figure 1.2**) with their associated growth conditions, characterized via ssNMR and cryo-electron microscopy (Cryo-EM).

The first high-resolution structure of an α -syn polymorph was reported by Tuttle et al. via solid-state NMR (2N0A).⁴¹ A fibril diameter of ~5 nm suggested a single elongated protofilament, however later review of the scanning transmission electron microscopy (STEM) analysis suggested double the diameter likely consisting of two protofilaments instead.⁴⁸ Most cryo-EM studies report fibrils composed of protofilament dimers, with a diameter of ~10 nm (~5 nm per protofilament), with distinct interfaces stabilized by a hydrophobic steric zipper or salt-bridge(s).^{49,47,50,51} Li et al. published two

distinct polymorphs consisting of two protofilaments under Cryo-EM, including the Greek-key containing 'rod' polymorph (6CU7) and bent β -arch 'twister' polymorph (6CU8), where the 'rod polymorph' takes a form similar to the general fibril structure, the twister is comprised only of a single hairpin extending to E83.⁵¹ Reported polymorphs with solved structures include those both grown from recombinant protein in vitro as well as from patient samples for both sporadic PD and MSA, both of which are consistent with the Greek-key motif yet producing polymorphs distinct from in-vitro strains.^{52,53} Several other dimer structures solved via Cryo-EM have also been published, including N-terminally acetylated and truncated versions of α -syn fibrils (**Table 1.1**).

Study	PDB	Polymorph	Buffer conditions	pH
(Tuttle et al., 2016) ⁴¹	2N0A	Full-Length	50 mM sodium phosphate 0.12 mM EDTA 0.02% sodium azide (w/v)	7.4
(Li et al., 2018) ⁵⁰	6A6B	N-terminal acetylated	50 mM Tris, 150 mM KCl, 0.05% NaN ₃	7.5
(Guerrero-Ferreira et al., 2018) ⁴⁹	6H6B	Truncated (1-121)	DPBS (Gibco) 2.66 mM KCl, 1.47 mM KH ₂ PO ₄ , 137.93 mM NaCl, 8.06 mM Na ₂ HPO ₄	7-7.3
(Li et al., 2018) ⁵¹	6CU7 6CU8	Rod polymorph 1A Twister polymorph 1B	15 mM tetrabutyl- phosphonium bromide	N/A
(Guerrero-Ferreira et al., 2018) ⁴⁷	6SSX 6SST	Polymorph 2A Polymorph 2B	50 mM Tris-HCl 150 mM KCl	7.5
(Ni, Xiaodan et al., 2019) ⁵⁴	6OSJ 6OSL 6OSM	Acetylated (1-140) Acetylated (1-122) Acetylated (1-103)	10 mM NaPi, 140 mM NaCl	7.4
(Schweighauser, et al., 2020) ⁵³	6XYO 6XYP 6XYQ	MSA Case 1 (Type 1) MSA Case 2 (Type II1) MSA Case 2 (Type II2)	30 mM Tris-HCl buffer	7.5

Table 1.1: List of Cryo-EM and SSNMR fibril structures and associated fibril growth conditions.

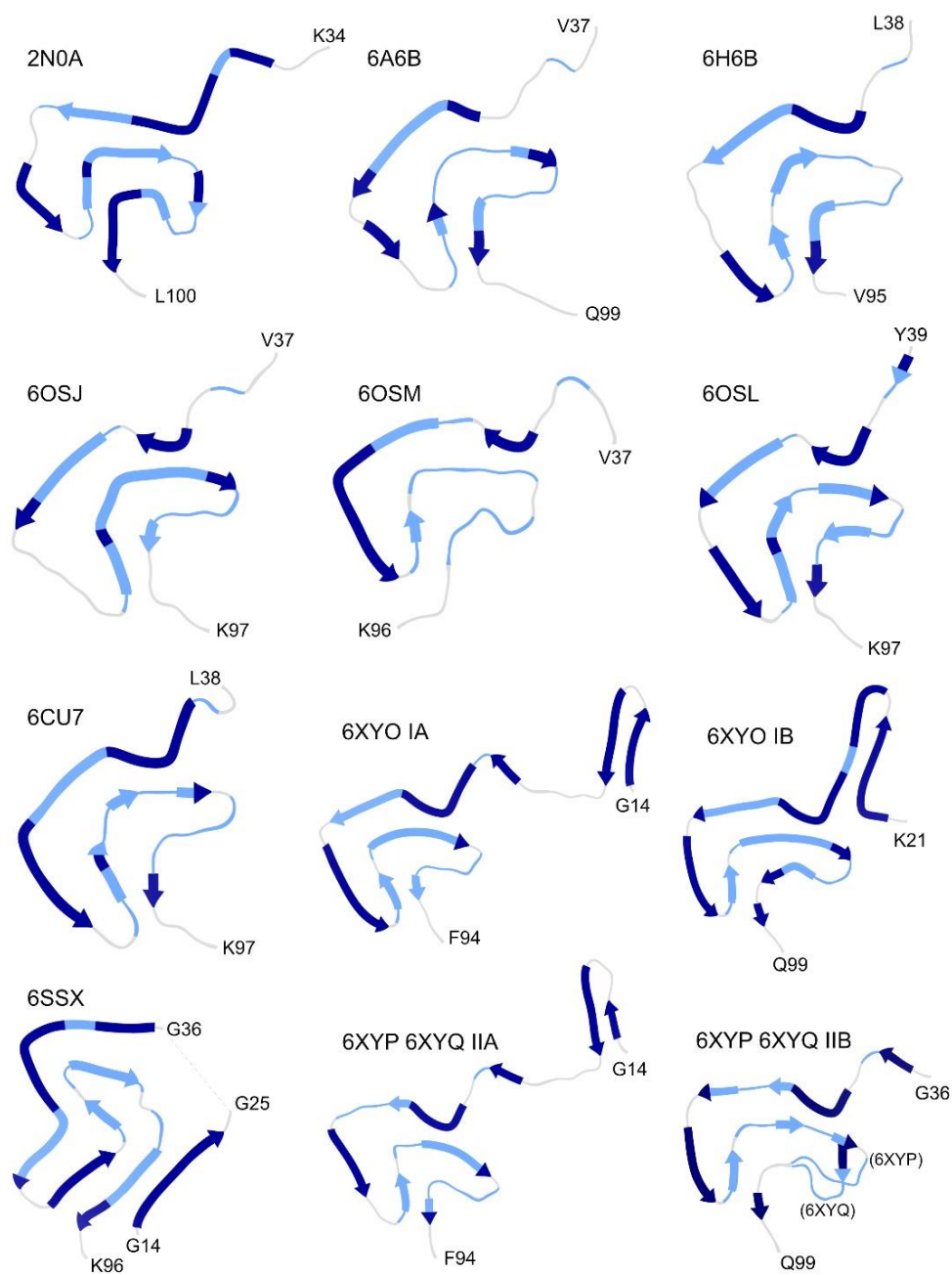


Figure 1.2: Structures of published WT α -syn protofilament cores with associated secondary structure elements labelled by their associated RCSB Protein Data Bank code (PDB). Thick arrows indicate β -strands, with light blue indicating all assigned residues of the fibril form determined in Chapter 4.2.1 of this thesis (G41-S42, G51-A56, G68-V71, G73-K80, and E83-A90) while dark blue and grey indicate all others (β -strands and loop regions respectively).

Although many in-vitro polymorphs maintain a mostly unstructured N-terminus, several other studies have shown otherwise. For example, a polymorph studied via NMR is suggested to have an entirely β -sheet structured N-terminus.⁴⁰ Additionally, another polymorph studied via ssNMR and cryogenic electron microscopy (Cryo-EM) indicates partial N-terminal binding to the periphery of the fibril core.^{47,55} Patient samples from PD and MSA show polymorphs distinct from those grown in-vitro with variability between cases, including a strongly interacting N-terminus in one of several such polymorphs.^{52,53} Another three new polymorphs obtained from PD and MSA patient samples via PMCA (protein misfolding cyclic amplification)⁵⁶ also exhibit a bound N-terminus in addition to an associated C-terminus bound to the fibril core.⁵⁷ They report rigid association of residues 124-134, while residues 98-123 remained unresolved.

1.3 Investigating protein structure using NMR

As discussed in chapter 1.1, the refolding effect on α -syn fibrils via externalized CL is of much interest but has only been studied via CD spectroscopy, following only the transition of secondary structure from the β -sheet fibrillar form to the α -helical lipid-bound monomer. In this thesis, we wish to confirm fibril refolding via exposure to CL and whether this effect is CL specific or an effect of anionic lipids in general. More specifically, we wish to track conformational changes in the fibril form when exposed to anionic lipids and to characterize the refolded form, ultimately coming to a better understanding of the mechanisms behind fibril-lipid interactions. To accomplish this, we

utilize NMR to first characterize the membrane-bound and fibril conformations to use as a roadmap to site-specifically track the changes between the fibril and lipid-refolded state.

NMR is a powerful tool for characterizing protein conformations at atomic level while maintaining their native-like environment. Magic angle spinning (MAS) and ssNMR are required for proteins which are insoluble, lipid-bound, or aggregates such as amyloid fibrils due to restricted mobility and tumbling given their size and rigidity, making them less amenable to regular solution NMR techniques.⁵⁸ Both the chemical environment and local structure directly affect the chemical shifts of nuclear spins allowing for site-specific residue chemical shift assignment and determination of general residue-specific secondary structure.⁵⁹ This is incredibly useful in the case of α -syn as each notable conformation exhibits unique secondary structure, from the α -helix of the membrane-bound form to the β -sheet NAC core of fibrils, with varying random coil regions between conformations.

In short, the structural diversity of the several conformations of α -syn are accessible through varying NMR techniques, allowing for the direct observation of either the flexible or structured regions by capitalizing on specific nuclear spin interactions discussed in Chapter 2. These ssNMR techniques can thereby monitor the transition from β -sheet fibrils to α -helically lipid-bound α -syn site-specifically, improving on previously published CD results which track only the overall secondary-structure transitions between states. NMR allows for the site-specific tracking of these conformational transitions induced via protein-lipid interactions to structurally

characterize the refolded state. The research plan regarding the samples required to follow such transitions are discussed in Chapter 4. In short, we compare samples containing either 1) monomeric α -syn bound to anionic lipid containing vesicles, 2) fibrils alone, or 3) fibrils bound to anionic lipid containing vesicles using ssNMR. This research marks important steps toward gaining further insight into the nature of interactions between fibrils and anionic lipid membranes.

2 Theory and Application of Protein Solid State Nuclear Magnetic Resonance

2.1 NMR Spectroscopy

The following discussion of the basics of NMR spectroscopy draws from multiple textbooks.^{60–63} NMR spectroscopy takes advantage of the intrinsic spin angular momentum of atomic nuclei via the use of a strong static external magnetic field and radio-frequency (RF) pulses. Spin $\frac{1}{2}$ nuclear spins are the simplest NMR-sensitive structural probes, with biological molecules containing ^1H , ^{13}C and ^{15}N spin $\frac{1}{2}$ nuclei. While ^1H is naturally abundant at 99.99%, the natural abundance of ^{13}C and ^{15}N are only 1.1% and 0.37% respectively, making it customary to enrich biological samples with these isotopes.^{61,63} In the most widely used *E. coli* cultures, isotopic labeling can be achieved via cell growth in M9 minimal media where the sole carbon and nitrogen sources such as glucose and ammonium chloride, are uniformly ^{13}C -enriched and ^{15}N -enriched, respectively. An isotopically enriched sample is placed in an external magnetic field which induces a non-zero nuclear equilibrium magnetization; RF pulses perturb a spin system from its equilibrium state, thereby resulting in the free induction decay (FID) response. The FID is acquired, and Fourier transformed to the frequency domain, resulting in a frequency spectrum with multiple lines, in which each peak corresponds to a specific atom in a molecule.

The spin angular momentum noted $\vec{I} = (I_x, I_y, I_z)$, has a total magnitude of

$$|\vec{I}| = [\vec{I} \cdot \vec{I}]^{1/2} = \hbar[I(I + 1)]^{1/2}, \quad (2.1)$$

where \hbar is the reduced Planck's constant. Placing spins in a strong magnetic field with a

direction chosen to be along the z-axis, $\vec{B}_0 = (0, 0, B_0)$, results in a quantized z-component of the spin angular momentum:

$$I_z = \hbar m \quad (2.2)$$

Here, m is the magnetic quantum number with allowed $(2I + 1)$ values of:

$$m = -I, -I + 1, \dots, I - 1, I. \quad (2.3)$$

Nuclei with non-zero spin angular momentum have a magnetic moment which is proportional to the spin angular momentum:

$$\vec{\mu} = \gamma_I \vec{I}. \quad (2.4)$$

The z-component quantization of the angular momentum in the external magnetic field is defined as *Zeeman splitting*, which in the case of spin $\frac{1}{2}$ nuclei ($I = \frac{1}{2}$) results in two states; the spin-up ($m = \frac{1}{2}$) and spin-down states ($m = -\frac{1}{2}$) correspond to the eigenstates of the Zeeman Hamiltonian described as:

$$H_Z = -\hbar \gamma_I B_0 I_z. \quad (2.5)$$

Here, the gyromagnetic ratio (γ_I) of the spin I is a constant of proportionality specific to each nucleus, with the magnitude determining the receptivity of said nucleus to NMR.

Following from Eq. 2.2 to 2.5, the quantization of the spin angular momentum z-component with respect to B_0 gives rise to two distinct energy levels:

$$E = \mp \frac{\hbar\gamma_I}{2} B_0. \quad (2.6)$$

Due to this energy difference, there is a slight difference between population of the up state ($N_{1/2}$) and population of the down state ($N_{-1/2}$) states, with the lower energy state having the higher population. For a sample of N spins at thermal equilibrium, the relative populations can be expressed via the Boltzmann distribution:

$$\frac{N_{1/2}}{N_{-1/2}} = \exp\left(\frac{\hbar\gamma_I B_0}{k_B T}\right) \quad (2.7)$$

The non-zero population difference results in an overall magnetization (M_0) of the sample parallel to the magnetic field along the z-axis, and at high temperatures ($\frac{\hbar\gamma_I B_0}{k_B T} \ll$

1) it can be approximated as:

$$M_0 = \frac{\hbar\gamma_I}{2} (N_{1/2} - N_{-1/2}) \approx \frac{\hbar^2 \gamma_I^2 B_0}{4k_B T} N. \quad (2.8)$$

While the population difference between the two states is small under most experimental conditions, a larger sample size and an increased number of spins N , lower temperature, higher field strength and higher gyromagnetic ratio would maximize the sensitivity of NMR experiments.

The difference in energy between the two states in Eq. 2.6 expressed in frequency units is known as the Larmor frequency, and it corresponds to the frequency of free precession of the magnetic moment about the static magnetic field z-axis:

$$\omega_0 = -\gamma B_0. \quad (2.9)$$

An RF-modulated electric current applied at or close to the Larmor frequency in a solenoid coil wrapped around the sample, generates a magnetic field within the solenoid which perturbs bulk magnetization M_0 from its equilibrium state along z-axis and rotates it into the transverse plane. Following the RF excitation, the non-equilibrium magnetization will precess at the Larmor frequency about the z-axis as described in Eq. 2.9. Such precession results in a time-dependent magnetic flux, which by way of Faraday's law induces a time-dependent current in the coil. This time-dependent current is the sinusoidal free-induction decay (FID), and its Fourier transform results in a spectrum with a peak at the Larmor frequency of the observed nuclei.

2.2 NMR Interactions

In addition to the strongest Zeeman interaction with the static external magnetic field (H_Z), nuclear spins are subjected to numerous other "internal" interactions defined by molecular structure. The total nuclear spin Hamiltonian describing an NMR experiment is therefore the sum of each of these interactions, taking the form:

$$H = H_Z + H_{CS} + H_D + H_J + H_{RF}. \quad (2.10)$$

The chemical shift (H_{CS}) is the result of shielding of nuclear spins by nearby electrons from the external magnetic field. The dipolar coupling (H_D) is a direct through-space interaction between individual nuclear magnetic moments, whereas J-coupling (H_J) is a spin-spin interaction mediated through bonds. Additionally, the external

interaction between applied RF magnetic fields and magnetic moments (H_{RF}) allows for manipulation of the individual internal interactions and is used for excitation of the NMR signal (FID), for inducing polarization transfers between spins and for removal of spin interactions, when necessary, i.e., decoupling. Under high fields the Zeeman interaction is the largest by several orders of magnitude, leaving only secular terms that commute with the Zeeman interaction to produce significant effects. The secular approximation accounts only for these terms and will be utilized in the following discussions of each term of the Hamiltonian.

2.2.1 Chemical Shift

The chemical shift is a change in the Larmor frequency which arises due to “nuclear shielding.” The external magnetic field interacts with the electrons surrounding the nuclear spin causing them to form auxiliary magnetic fields of their own, counteracting the external field and effectively ‘shielding’ the nuclear spin from the external field.⁶¹ Given that the electron density distribution is anisotropic, the chemical shift is itself anisotropic. The general chemical shift Hamiltonian is given as:⁶²

$$H_{CS} = -\gamma \vec{I} \hat{\sigma} \vec{B}. \quad (2.11)$$

where \vec{I} and \vec{B} vectors define the nuclear spin and external magnetic field, while the shielding is defined via $\hat{\sigma}$, the nuclear shielding tensor:

$$\hat{\sigma} = \begin{pmatrix} \sigma_{xx} & \sigma_{xy} & \sigma_{xz} \\ \sigma_{yx} & \sigma_{yy} & \sigma_{yz} \\ \sigma_{zx} & \sigma_{zy} & \sigma_{zz} \end{pmatrix} \quad (2.12)$$

This second rank tensor is diagonal in the special frame, the 'principal axis system' (PAS), with principal components denoted as σ_{11} , σ_{22} , and σ_{33} . In isotropic liquid samples, rapid tumbling of molecules in solution averages out the anisotropy, resulting in the isotropic shielding constant:⁶²

$$\sigma_{ISO} = \frac{\sigma_{11} + \sigma_{22} + \sigma_{33}}{3}. \quad (2.13)$$

In the solid state, such as samples where molecules are immobilized and do not undergo fast tumbling and lack a particular orientation (e.g., unoriented membrane-bound proteins, fibrils, etc.), the chemical shift anisotropy is not averaged out, thereby leading to spectral broadening due to orientation dependence. The chemical shift anisotropy (CSA) is defined as:^{64,65}

$$\sigma_{CSA} = \sigma_{33} - \sigma_{ISO}. \quad (2.14)$$

The associated asymmetry of the tensor defined as:

$$\eta = \frac{(\sigma_{22} - \sigma_{11})}{\sigma_{CSA}}. \quad (2.15)$$

Together, the chemical shift Hamiltonian can be represented as the combination of the two terms:⁶²

$$H_{CS} = -\gamma B_0 \sigma_{ISO} I_z - \gamma B_0 \sigma_{CSA} \frac{1}{2} (3 \cos^2 \theta - 1 + \eta \sin^2 \theta \cos 2\varphi) I_z. \quad (2.16)$$

Where θ and φ are the angles between the PAS and the static magnetic field along the z-direction, defining the orientation dependence of the sample.

Since the resulting resonant frequencies are proportional to the magnetic fields used, it is customary when measuring chemical shifts of nuclear spins to express them in parts per million (ppm), referenced to some standard. For protein NMR it is recommended to use 2,2-dimethyl-2-silapentane-5-sulfonate, sodium salt (DSS) as the standard reference compound.^{66,67,68}

2.2.2 Dipolar Coupling

The next internal interaction is the anisotropic through-space dipolar coupling between two magnetic dipoles (dipole-dipole interaction). The Hamiltonian representing this direct interaction between two nuclei \vec{I} and \vec{S} is as follows:^{60,62,63}

$$H_{D,IS} = b_{IS} \cdot \left(3 \left(\vec{I} \cdot \frac{\vec{r}_{IS}}{r_{IS}} \right) \left(\vec{S} \cdot \frac{\vec{r}_{IS}}{r_{IS}} \right) - \vec{I} \cdot \vec{S} \right). \quad (2.17)$$

The vector connecting the two nuclear spins is \vec{r}_{IS} , while r_{IS} represents the internuclear distance between them. The dipolar coupling constant (b_{IS}) between spins \vec{I} and \vec{S} is defined as:⁶³

$$b_{IS} = -\frac{\mu_0 \gamma_I \gamma_S \hbar}{4\pi r_{IS}^3} \quad (2.18)$$

where μ_0 is the permeability of free space, and γ_I and γ_S are the gyromagnetic ratios of spins I and S , respectively. Under the high field secular approximation, the dipolar coupling Hamiltonian can be rewritten for homonuclear coupling (same isotopic species, I_i and I_j) and heteronuclear coupling (different isotopic species, I and S) as:⁶²

$$H_{D,II} = \frac{b_{II}}{2} (3 \cos^2 \theta_{ij} - 1) (3I_{iz}I_{jz} - \vec{I}_i \cdot \vec{I}_j) \quad (2.19)$$

$$H_{D,IS} = \frac{b_{IS}}{2} (3 \cos^2 \theta_{IS} - 1) 2I_z S_z. \quad (2.20)$$

Both are anisotropic, depending on the angle θ_{IS} (or θ_{ij}) between the connecting vector \vec{r}_{IS} (or \vec{r}_{ij}) and the magnetic field \vec{B}_0 , leading to anisotropic spectral broadening in powdered samples. Similar to the CSA, this interaction is averaged out by fast molecular tumbling if such tumbling is present, but it remains largely intact in the solid state, resulting in anisotropic line broadening. The use of MAS allows for eliminating of the anisotropic broadening as discussed in section 2.3.

2.2.3 J-Coupling

The through-bond J-coupling interaction, also referred to as scalar coupling, involves the interaction between two nuclear spins mediated through bonds (as opposed to the through-space dipolar interaction). The Hamiltonian for the interaction between a pair of spins I and S (both homo- and heteronuclear) can be approximated as:⁶²

$$H_J = 2\pi J_{IS} I_z S_z \quad (2.21)$$

where J_{IS} represents the J-coupling constant between the interacting nuclei. J-couplings are largely isotropic, allowing for their observation as the symmetric splitting of a peak based on the number of associated bonds. While weak in comparison to the previously

discussed interactions, it is the primary means of polarization transfer between nuclear spins in solution NMR, as well as between spins within mobile protein fragments in the solid state.

2.3 Magic Angle Spinning

In solution, the anisotropic broadening associated with chemical shift anisotropy and dipolar interactions is averaged out due to fast molecular tumbling. The same cannot be said for motionally restricted molecules in which the anisotropic interactions prevail, resulting in broadened peaks and an overall decrease in spectral resolution (**Figure 2.2a**).⁶⁹ While molecular weight of a molecule limits applicability of solution NMR due to reduced tumbling in larger molecules, solid-state NMR has no such restriction under the use of MAS.^{62,64}

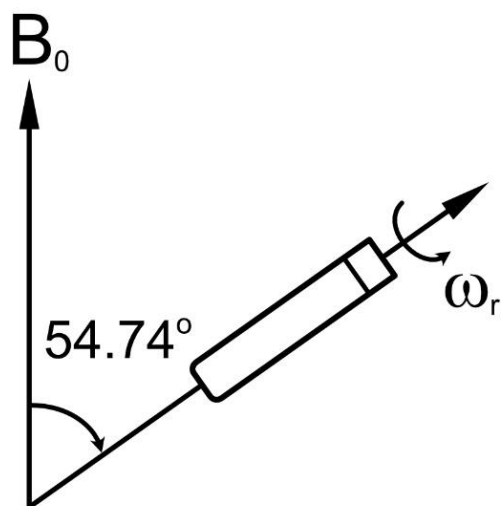


Figure 2.1 - Magic Angle Spinning NMR experiment. The sample is packed into a cylindrical rotor which is spun at a frequency of ω_r about an axis oriented at the magic angle of 54.74° with respect to the external magnetic field.

MAS allows for the removal of anisotropy in solid samples.^{70,71} The sample is packed into a rotor and spun around an axis pointing at the “magic” angle of 54.74° relative to the external magnetic field, as shown in **Figure 2.1**, thereby introducing a periodic time-dependence to the anisotropic chemical shift and dipolar Hamiltonians:⁷²

$$H_{CS,I} = \omega_{CS,I}(t)I_z \quad (2.22)$$

$$H_{D,II} = \omega_{D,II}(t)(3I_{iz}I_{jz} - \vec{I}_i \cdot \vec{I}_j) \quad (2.23)$$

$$H_{D,IS} = \omega_{D,IS}(t)I_z S_z. \quad (2.24)$$

The time modulated dipolar frequencies for the heteronuclear dipolar interaction case can be written as:⁷²

$$\omega_{D,IS}(t) = b_{IS}(g_0 + g_1 \cos(\omega_r t + \varphi_{IS}) + g_2 \cos(2\omega_r t + 2\varphi_{IS})) \quad (2.25)$$

Where the polar coordinate angles θ_{IS} and φ_{IS} define the internuclear vector with respect to the rotation axis at $t=0$, and θ_R represents the magic angle relative to the z-axis. This can be rewritten for the homonuclear case, $\omega_{D,IS}(t)$, given proper parameter substitution as in Eqs. 2.19-2.20. The time dependent coefficients are defined as:

$$g_0 = -\frac{(3 \cos^2 \theta_R - 1)(3 \cos^2 \theta_{IS} - 1)}{2} \quad (2.26)$$

$$g_1 = \frac{3}{4}(\sin 2\theta_R)(\sin 2\theta_{IS}) \quad (2.27)$$

$$g_2 = -\frac{3}{4}(\sin^2 \theta_R)(\sin^2 \theta_{IS}) \quad (2.28)$$

A similar breakdown can be shown for the chemical shift anisotropy (CSA) under MAS. Firstly, the time dependency of the CSA strength is given by the following:

$$\omega_{CS,I}(t) = \omega_0 \sigma_{ISO} + \omega_0 \sigma_{CSA}(g_0 + g_1 \cos(\omega_r t + \psi_1) + g_2 \cos(2\omega_r t + 2\psi_2)) \quad (2.29)$$

With σ_{ISO} and σ_{CSA} as previously described. The Euler angles α , β , γ describing the orientation of the PAS of the chemical shift tensor with respect to the rotor frame, the g_0 , g_1 , g_2 , ψ_1 and ψ_2 coefficients are given as:

$$g_0 = -\frac{(3 \cos^2 \theta_R - 1)}{2} \left\{ \frac{(3 \cos^2 \beta - 1)}{2} + \frac{\eta}{2} \sin^2 \beta \cos 2\gamma \right\} \quad (2.30)$$

$$g_1 = -\frac{1}{2} \sin 2\theta_R \sin \beta \{(\eta \cos 2\gamma + 3)^2 \cos^2 \beta + \eta^2 \sin^2 2\gamma\}^{1/2} \quad (2.31)$$

$$g_2 = \frac{1}{2} \sin^2 2\theta_R \left\{ \left[\frac{3}{2} \sin^2 \beta - \frac{\eta}{2} \cos 2\gamma (1 + \cos^2 \beta) \right]^2 + \eta^2 \cos^2 \beta \sin^2 2\gamma \right\}^{1/2} \quad (2.32)$$

$$\psi_1 = \alpha + \tan^{-1} \left\{ \frac{\eta \sin 2\gamma}{(\eta \cos 2\gamma + 3) \cos \beta} \right\} \quad (2.33)$$

$$\psi_2 = 2\alpha + \tan^{-1} \left\{ \frac{-\eta \cos \beta \sin 2\gamma}{\frac{3}{2} \sin^2 \beta - \frac{\eta}{2} \cos 2\gamma (1 + \cos^2 \beta)} \right\} \quad (2.34)$$

The g_0 coefficients in Eq. 2.26 and 2.30 describe the static anisotropic line broadening under MAS conditions. It can be eliminated by setting the angle θ_R to the magic angle value of 54.74° :

$$\theta_R = \arccos\left(\frac{1}{\sqrt{3}}\right) \approx 54.74^\circ. \quad (2.35)$$

The remaining time-dependent terms oscillate with frequencies of ω_r and $2\omega_r$ and are therefore effectively averaged to zero over a multiple of complete rotor periods, or at a sufficiently fast spinning frequency greater than the strength of the anisotropy. Therefore, under MAS only the isotropic contributions to the spectral frequencies remain, resulting in peaks at the isotropic chemical shifts. **Figure 2.2** illustrates the effect of MAS on the ^{31}P NMR spectra of barium diethylphosphate powder.

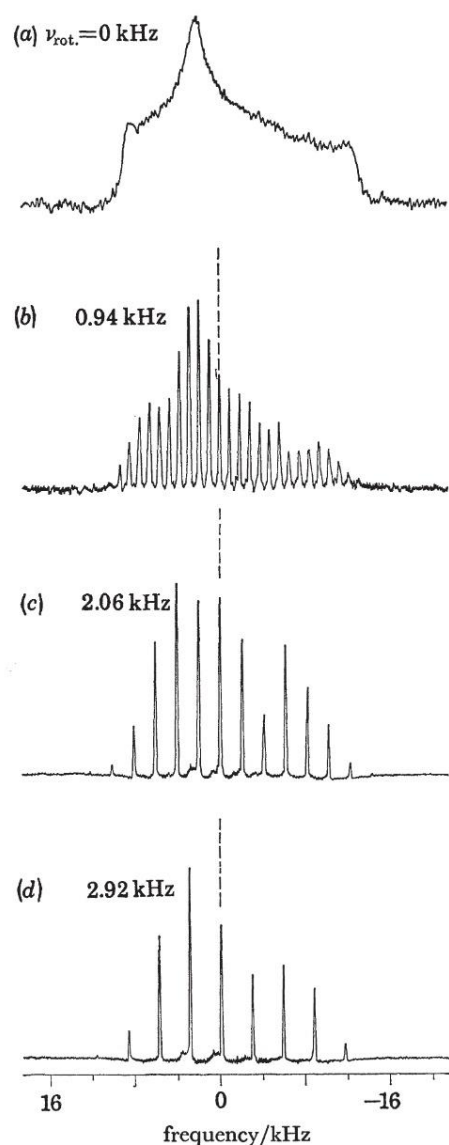


Figure 2.2 - ^1H decoupled ^{31}P MAS spectra of barium diethylphosphate (BDEP) with increasing ω_r . Starting with (a) $\omega_r = 0$, an axially asymmetric spectrum, increasing to (d) 2.92 kHz MAS frequency, highlighting the removal of anisotropic broadening. The dashed line indicates the isotropic shift. Reprinted by permission from The Royal Society: Philos Trans R Soc Lond B Biol Sci. "Magic angle sample spinning in inhomogeneously broadened biological systems." Herzfeld J, Ruffosse A, Haberkorn RA, Griffin RG, Glimcher MJ, 1980, 289(1037):459-69.⁶⁹

2.4 Multidimensional NMR

With the addition of MAS and its removal of anisotropic broadening, increasing resolution may still prove necessary. This is especially so for larger and more heterogenous samples where natural line broadening, spectral crowding and degeneracy are commonplace. Simple 1D NMR experiments become insufficient for resolving the large number of observed nuclei. To obtain site-specific resolution in these cases, multidimensional NMR provides a means of separating chemical shifts.⁶¹

The general scheme for a two-dimensional (2D) NMR experiment is represented in **Figure 2.3** by four distinct steps: excitation, evolution (t_1), mixing, and acquisition (t_2). During excitation, the spin system is perturbed from its thermal equilibrium via the application of RF pulses. Next, the spins evolve under the isotropic chemical shifts for a fixed period t_1 . Following t_1 evolution is the mixing period, during which polarization is transferred between the coupled spin species of interest by means of additional RF pulses and/or time delays; the mixing is followed by the direct detection (t_2). The experiment is repeated as a function of t_1 , varied from zero to a certain $t_{1\max}$ value. The acquired signal $S(t_1, t_2)$ is therefore a function of the incremented indirect evolution t_1 , and the directly detected t_2 . Double Fourier transform of $S(t_1, t_2)$ results in a 2D spectrum with indirect dimension and direct dimension in the frequency domain $S(\delta_1, \delta_2)$, as can be seen in **Figure 2.4A**. The 2D can be extended to a three-dimensional (3D) experiment with the addition of a third time dimension and mixing/evolution step, further increasing resolution (**Figure 2.4B**).



Figure 2.3 - Generalized scheme for a 2D NMR pulse sequences utilizing RF pulses. Each of the four distinct steps are indicated, including excitation and mixing; both of which include the use of various RF pulses and delays.

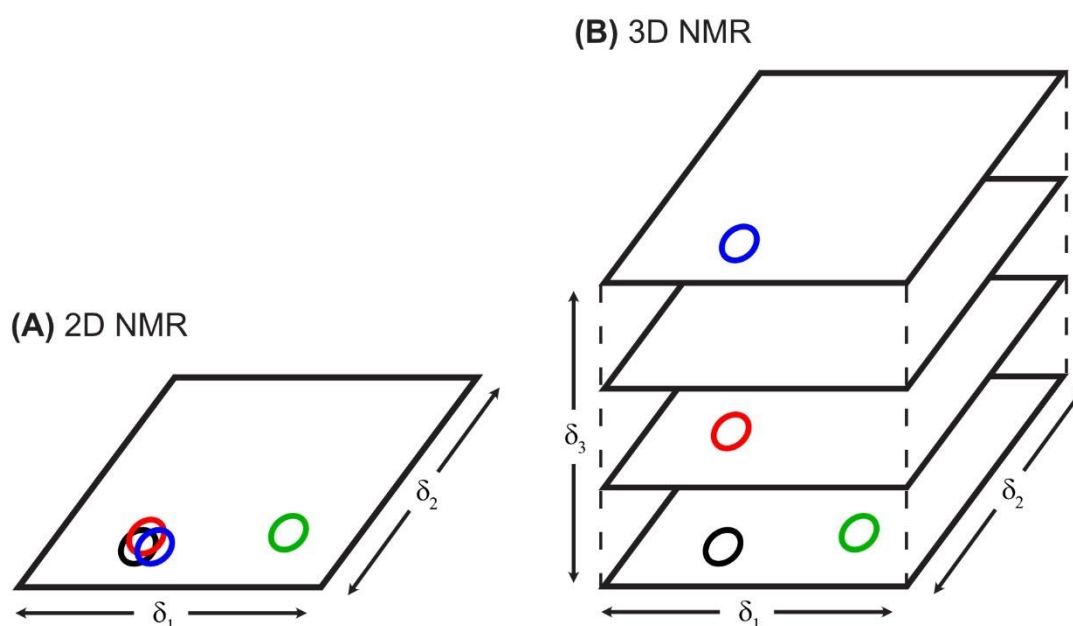


Figure 2.4 - Multidimensional NMR spectra of (A) a 2D unresolved spectra and (B) a resolved 3D spectrum, where peaks are represented by a single contour line with nearly identical chemical shifts in the δ_1 and δ_2 dimensions. While the 2D is spread across its two independent frequency axes δ_1 and δ_2 corresponding to the indirect evolution t_1 and the directly detected t_2 , the 3D contains two indirect evolution periods t_1 and t_2 , with acquisition in the direct dimension t_3 . While the green peak is already resolved in the 2D spectra, the addition of a third dimension (δ_3) allows for resolution of black, red & blue peaks overlapped in the 2D spectra, as illustrated by the separation of each coloured peak in the 3D.

Multidimensional heteronuclear experiments allow for the separation of ^1H , ^{13}C and ^{15}N chemical shifts into multiple dimensions via multiple polarization transfer steps between neighboring atoms. Depending on the internal and global mobility of a protein, these polarization transfers can take advantage of either dipolar couplings using the cross-polarization technique (CP)⁷³ and other dipolar recoupling techniques such as dipolar-assisted rotational resonance (DARR),^{73,74} or via J-couplings using the Inensitive Nuclei Enhanced by Polarization Transfer approach (INEPT)⁷⁵ and other methods taking advantage of scalar couplings, all of which are further explained in chapter 2.5. Molecules studied under NMR can be characterized by regions of differential mobility, containing both rigid and mobile fragments which can be studied separately via NMR. CP is much more efficient at exciting spins and transferring polarization in rigid fragments of a molecule, whereas INEPT can efficiently excite and transfer polarization between heteronuclear spin species in mobile molecular fragments. An example of increased spectral resolution achieved via higher dimensional heteronuclear experiments is shown in **Figure 2.5** for a sample of lipid-bound α -syn, from a 1D INEPT ^{13}C spectrum (**Figure 2.5A**), to a 2D spectrum (**Figure 2.5B**) which uses INEPT for excitation of carbons and TOBSY (total through-bond correlation spectroscopy)⁷⁶ for transferring polarization between them. While 1D ^{13}C spectrum contains overlapped signals from multiple residues, multiple backbone and sidechain atoms become resolvable in the 2D ^{13}C - ^{13}C correlation spectrum (**Figure 2.5B**).

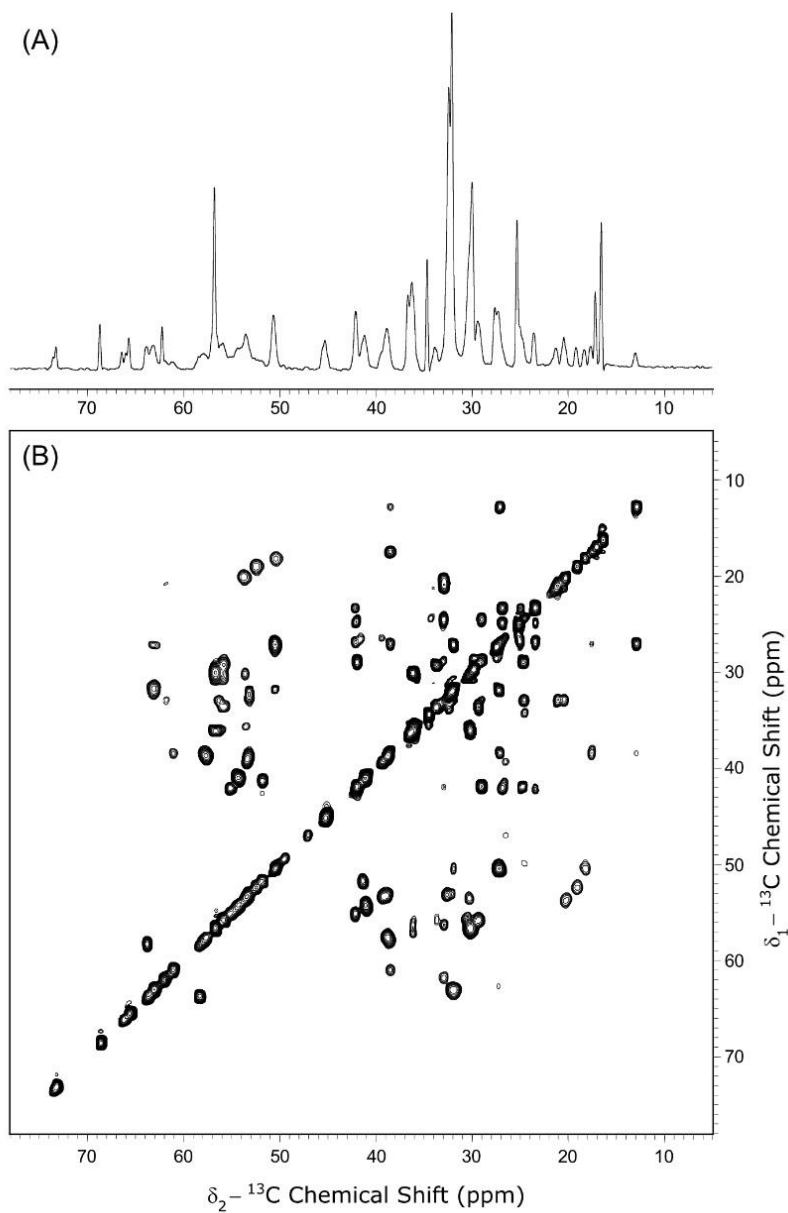


Figure 2.5 - Increasing resolution via multidimensional NMR from a (A) 1D $^1\text{H}/^{13}\text{C}$ INEPT to a 2D INEPT TOBSY ^{13}C - ^{13}C correlation spectra (B). The 1D spectrum contains multiple overlapped signals which become resolved in a 2D spectrum. The experiments were run at a proton frequency of 800.23 MHz and a spinning frequency of 14.3 kHz, a TOBSY mixing time of 7.133 ms was used in the 2D experiment.

2.5 “Mobility” filter – INEPT vs CP excitation

Over time, the FID collected following excitation must decay back to zero as the spins relax to their thermal equilibrium state along the z-axis. This occurs through two processes: longitudinal relaxation (T_1) and transverse relaxation (T_2).^{61,63} The longitudinal relaxation time indicates how long the spin ensemble will take to reach thermal equilibrium along the z-axis, whereas the transverse relaxation T_2 time indicates the loss of coherence in the transverse plane. Both are related to the thermal motions of the excited atoms as well as anisotropic interactions, driving the system to thermal equilibrium based on the amplitudes and time scales of these motions. Importantly in the solid-state, T_2 must be replaced by the coherence lifetime T_2' which combines both the stochastic contribution of the transverse relaxation and the residual coherent contribution that arises from spin interactions which are incompletely averaged by MAS and decoupling.⁶³ The latter is much stronger and dominates the transverse relaxation processes in solids in most situations.

Proteins are structurally and dynamically diverse molecules. As pointed out above, they often contain both rigid regions undergoing only small amplitude motions, and more flexible portions which undergo faster motions often on larger length scales. Mobility directly effects coherence lifetimes (T_2') which increase if anisotropic effects such as dipolar couplings are averaged out by motions. This is similar to what occurs in the solution phase, where dipolar couplings and CSA are averaged out by isotropic motions and J-couplings become dominant. In contrast, dipolar couplings dominate in motionally restricted regions. As a result, the selective excitation and subsequent

observation of the rigid or flexible regions is possible using specific excitation and polarization transfer mechanisms. Cross-polarization⁷³ utilizes dipolar couplings for the excitation of rigid regions while the through-bond Inensitive Nuclei Enhanced by Polarization Transfer (INEPT)⁷⁵ utilizes J-couplings to selectively excite flexible regions. The pulse sequences for the CP and INEPT ^1H - $^{13}\text{C}/^{15}\text{N}$ heteronuclear transfers are shown in **Figure 2.6**; they transfer polarization via through-space and through-bond mixing, respectively. INEPT excitation can be combined with TOBSY (total through-bond correlation spectroscopy)⁷⁶ mixing in homonuclear 2D ^{13}C - ^{13}C chemical shift correlation experiments in combination to yield 2D spectra of mobile molecular fragments, whereas CP is combined with through-space mixing methods such as DARR (dipolar-assisted rotational resonance)^{73,74} to result in spectra corresponding to the rigid species. These methods and higher order heteronuclear correlation experiments are utilized for the assignment of the chemical shifts for proteins with diverse structure, allowing for site-specific analysis and tracking of conformational changes between samples. Methods regarding chemical shift assignments are explained in Chapter 3.3.

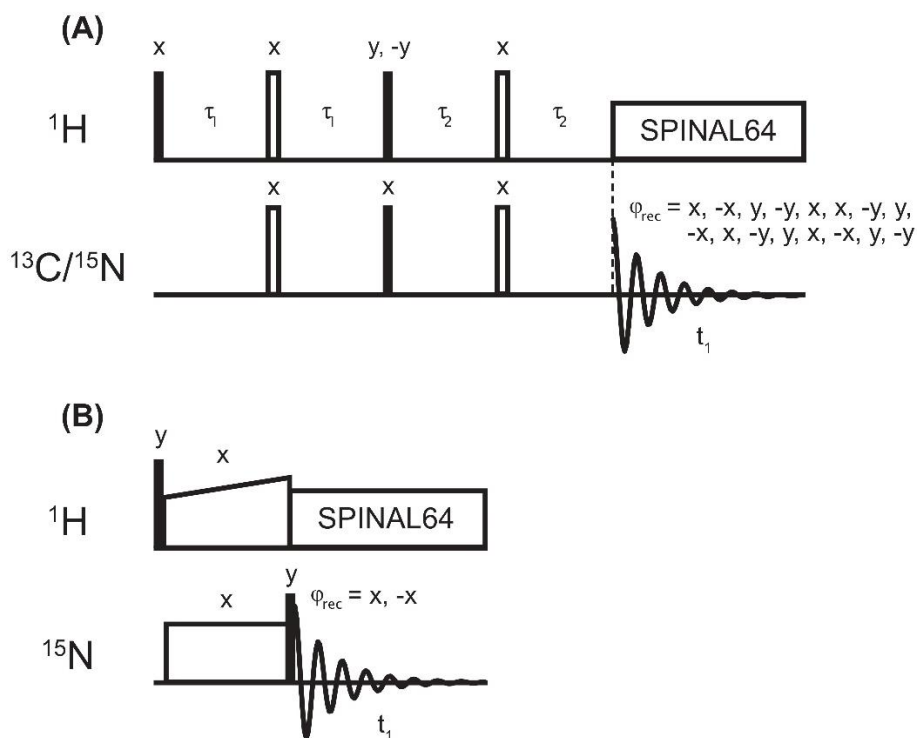


Figure 2.6 - The two 1D MAS solid-state NMR pulse sequences for excitation of (A) mobile species selectively excited using INEPT, and (B) rigid species selectively excited using CP. Within the INEPT sequence τ_1 and τ_2 are set to the J-coupling constant (J_{IS}) between heteronuclear spins I and S according to: $\tau_1 = 1/(4J_{IS})$ and $\tau_2 = 1/(6J_{IS})$, based on multiplicity (CH or CH₂, respectively) but values are generally optimized given strong T_2 effects.

2.6 Characterization of Protein Structure using NMR

Chemical shifts are the primary NMR observables. While chemical shifts are already generally distinct between nuclei of interest ($^1\text{H}^N$, $^1\text{H}^\alpha$, $^{13}\text{C}^\alpha$, $^{13}\text{C}^\beta$, etc., and ^{15}N), they can also be individually distinguished between like-nuclei due to the local structure and chemical and electrostatic environment around them. The characterization of biological molecules such as proteins by NMR involves understanding how the chemical

shift of the specific nuclear species is affected by local structure based on comparisons with known correlations. Both primary, secondary, and tertiary structure have significant and specific effects on the resulting chemical shifts. Firstly, the same nuclear species may have distinct chemical shift distributions. For example, the backbone carbonyls (180-170 ppm) have vastly different average chemical shifts than aliphatic carbons (ca. 70-10 ppm), which themselves have varying chemical shifts (ex. $^{13}\text{C}^{\alpha}$ vs $^{13}\text{C}^{\beta}$) as well as including significant differences between amino acids, data for which can be found on the Biological Magnetic Resonance Data bank.⁷⁷ Importantly, chemical shifts of backbone and some side chain atoms also depend on the secondary structure, i.e., α -helical, random coil, and β -sheet structure give rise to significant effects on the backbone atom and CB shifts within the same residue type. This is pertinent for our study of α -syn given the diverse secondary structure between its multiple conformations. The chemical shift index (CSI) and probability-based secondary structure identification present notable means for chemical shift based secondary structure analysis and identification.^{59,78} After assigning chemical shifts, such methods can be utilized to site-specifically interpret conformational changes.

Given the structural diversity of α -syn, which depending on the environment and interaction partners, may undergo conformational changes involving the formation of each type of secondary structure (e.g., random coil in the monomeric form, helical in the lipid-bound state and β -structure in fibrils), determining atom-specific chemical shifts requires utilizing separate assignment methods for both rigid and mobile regimes. Methods regarding chemical shift assignments and the corresponding experiments

required are explained in detail in section 3.3. With this, the structural characterization of the distinct monomer and fibril samples can be achieved, allowing for the site-specific tracking of conformational changes induced by protein-lipid or protein-protein interactions.

3 Materials and Methods

Common chemicals of a reagent grade for protein expression, isolation and reconstitution were purchased from either Fisher Scientific (Unionville, Ontario, Canada) or Sigma-Aldrich (Oakville, Ontario, Canada). ^{15}N -labeled ammonium chloride and uniformly ^{13}C -labeled (U- ^{13}C) glucose was purchased from Cambridge Isotope Laboratories (Andover, MA, USA). 1,2-dioleoyl-*sn*-glycero-3-phosphate (DOPA), tetraoleoyl cardiolipin (TOCL), and 1,2-dioleoyl-*sn*-glycero-3-phosphocholine (DOPC) were purchased from Avanti Polar Lipids (Alabaster, AL) as chloroform solutions (>99% purity) and used without further purification.

3.1 Expression and purification of α -synuclein

Uniformly ^{13}C , ^{15}N -labeled (UCN) α -syn was produced and purified according to previously published protocols with modifications for isotopic labelling.^{19,79} Briefly, wild-type α -syn (pET21a vector, purchased from Addgene – Plasmid 51486) was transformed into BL21-Codonplus (DE3)-RIPL competent cells (Life Technologies) and used to inoculate a 10 mL LB starter culture left to grow overnight in an incubator shaker at 37 °C. Afterward, the culture was diluted in 200 mL LB media and left to grow at 37 °C until an A_{600} of ~ 0.6 - 0.8 was reached. The culture was centrifuged at 2,500 x g for 10 min at room temperature and the resulting pellet was solubilized in M9 minimal media (1.5 L) supplemented with 1.0 g/L of $^{15}\text{NH}_4\text{Cl}$, 3.0 g/L of U- ^{13}C glucose, 2 mM MgSO_4 and 0.1 mM CaCl_2 , and again left in the incubator shaker at 37 °C until a target

density of $A_{600} \sim 0.6 - 0.8$ was reached. The cells were then induced with 250 $\mu\text{g/ml}$ IPTG for 3-5 hours, after which they were separated and centrifuged at 6000 rpm for 5 min at 4 $^{\circ}\text{C}$ using a JA-10 rotor; pellets were stored at -20 $^{\circ}\text{C}$ until ready for purification. Both LB and M9 growth media contained 50 $\mu\text{g/ml}$ ampicillin and 33 $\mu\text{g/ml}$ chloramphenicol. Purification was separated into two rounds. Briefly, half of the resulting pellets (from 750 ml culture) were thawed and homogenized in 50 mL water, sonicated for 5 minutes, then centrifuged, boiled, and centrifuged again (using a JA-25.5 rotor at 25,000rpm for 30 min at 4 $^{\circ}\text{C}$). The supernatant was filtered through a PVDF 0.22 μm membrane and topped up with 1 M Tris-HCl (pH 8.0) to reach a final concentration of 20 mM. Anion-exchange chromatography (FPLC) was then performed on a GE HiTrap DEAE FF 5 mL column connected to a DuoLogic system (Bio-Rad). SDS-PAGE was utilized to identify α -syn containing fractions. Those fractions were combined and subjected to several rounds of dialysis to reduce salt concentration to nanomolar levels before the next round of purification. Reversed-phase high-performance liquid chromatography (HPLC) was then performed for further purification using a Symmetry 300 (5 mm C_{18} , 4.6 x 250 mm) column on a Waters system with Millennium 32 software. A mobile phase of acetonitrile in water was used, linearly increasing the acetonitrile content from 30-50% (v/v) by 1 %/min over a total volume of 20 mL, with 0.1 % TFA as an ion pairing agent. The purified protein was then lyophilized and stored at -20 $^{\circ}\text{C}$ until further use.

3.2 Sample preparation for NMR studies.

Five samples were examined in this work (**Table 3.1**): (i) α -syn fibrils; (ii) α -syn fibrils bound to large unilamellar vesicles (LUV) made of anionic tetraoleoyl cardiolipin (TOCL) and 1,2-dioleoyl-*sn*-glycero-3-phosphocholine (DOPC) (41:59 molar ratio), at a protein to lipid ratio of 1:300 (sample called F:CL300 in the following); (iii) α -syn fibrils bound to LUVs consisting of anionic lipid 1,2-dioleoyl-*sn*-glycero-3-phosphate (DOPA) and DOPC at a 41:59 molar ratio, and at a protein to lipid ratio of 1:300 (F:PA300); (iv) monomeric α -syn bound to LUVs made of TOCL:DOPC (41:59 molar ratio) at a protein to lipid ratio of 1:100 (AS:CL100); (v) monomeric α -syn bound to LUVs consisting of DOPA:DOPC (41:59 molar ratio), at a protein to lipid ratio of 1:100 (AS:PA100).

Table 3.1 - Summary of samples used in this study.

SAMPLE	DETAILS
FIBRILS	In-vitro Fibrils, Control Sample
AS:CL100	Monomer AS bound to TOCL:DOPC liposomes (41:59 mol%), PLR* 1:100
AS:PA100	Monomer AS bound to DOPA:DOPC liposomes (41:59 mol%), PLR 1:100
F:PA300	Fibrils exposed to DOPA:DOPC liposomes (41:59 mol%), PLR (1:300)
F:CL300	Fibrils exposed to TOCL:DOPC liposomes (41:59 mol%), PLR (1:300)

*PLR, protein-to-lipid molar ratio.

3.2.1 Preparation of fibrils

Lyophilized UCN α -syn protein powder was diluted using 10 mM potassium phosphate buffer (pH 7.4) to prepare 500 μ L aliquots of monomeric α -syn at final protein concentrations of 5 mg/ml. Stock solution was first centrifuged at 100,000 x g at 4 °C for 60 min to remove any oligomers and the supernatant was taken to produce pre-formed fibrils (PFFs) by shaking on a Vibromixer at 1000 rpm for 7 days at 37 °C. Fibril samples were then centrifuged at 100,000 x g for 2 h and packed into a 3.2-mm thin-walled NMR rotor. The formation of fibrils was confirmed by sedimentation assay.

3.2.2 Liposome preparation

Large Unilamellar Vesicles (LUVs) of a 100 nm diameter were formed utilizing methods outlined by Mayer et al. (1986).⁸⁰ In short, aliquots of TOCL and DOPC, or DOPA and DOPC were combined in chloroform at a 41:59 molar ratio, mimicking the OMM surface charge after CL exposure. Lipid combinations were then dried under a stream of argon and put under vacuum for at least 12 hours. Following this, lipids were resuspended in water to a final concentration of 20-40 mM, thoroughly mixed via vortexing and freeze/thaw cycles, and extruded through a 100 nm filter 30 times until uniform in size. Size was verified prior to use by DLS (Dynamic Light Scattering) using a Malvern Zetasizer Nano ZS on 20-50 mM LUV samples. The TOCL:DOPC and DOPA:DOPC lipid composition were previously chosen as a simple model of the outer mitochondrial membrane under stress while mimicking its overall net charge in order to directly compare the effects of anionic lipid-specific effects.⁷⁹ As previously mentioned,

CL and PA are similar in that they have been shown to externalize from the IMM to the OMM as a result of mitochondrial stress (specifically via treatment of rotenone or staurosporine).²⁰

3.2.3 Preparation of proteoliposomes

Lyophilized monomeric UCN α -syn was dissolved in 10 mM potassium phosphate buffer (pH 7.4) at a concentration of 5 mg/mL and incubated with TOCL:DOPC or DOPA:DOPC LUVs at a PLR of 1:100 at 37 °C for 3 hours. Similarly, fibril samples were incubated with LUVs for 3 hours at a PLR of 1:300. Previous circular dichroism (CD) studies have shown that the conformational transition in fibrils induced by interactions with anionic lipids containing TOCL is nearly complete after 3 hours, and well within the plateau regime at PLR of 1:300.¹⁹ A protein-to-lipid ratio of 1:100, located at the start of the plateau regime, was used for the monomer:lipid samples in order to compensate for their slightly higher mobility which results in lower sensitivity to NMR measurements.¹⁹ Proteoliposomes were pelleted at 900,000 x g for 18 hours and packed into a 3.2-mm thin-walled NMR rotor. Estimated protein content was ~4-5 mg in the proteoliposome samples.

3.3 Solid-State NMR experiments

All magic angle spinning (MAS) NMR experiments were collected on a Bruker Avance III spectrometer operating at a magnetic field strength of 18.8 T corresponding

to a proton Larmor frequency of 800.230 MHz, using a Bruker Efree $^1\text{H}/^{13}\text{C}/^{15}\text{N}$ 3.2 mm and TL2 MAS probes. The MAS frequency was set to 14.3 kHz, and the temperature was maintained at 5 °C for all experiments. Chemical shifts were referenced indirectly to DSS (2,2-Dimethyl-2-silapentane-5-sulfonic acid) by using adamantane as secondary reference.^{66,68} Data were processed in NMRpipe and analysed in CARRA.^{82,83}

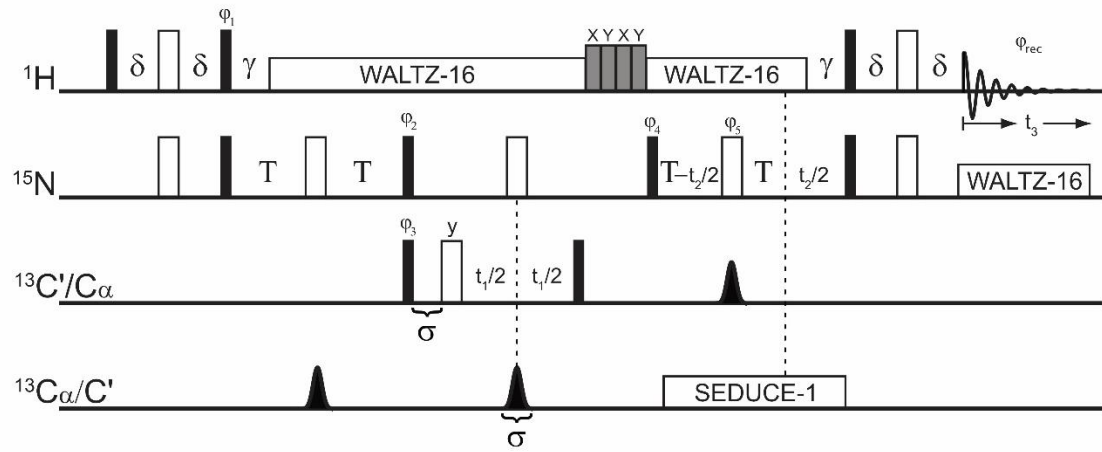
3.3.1 ^1H detected NMR experiments

Four 3D proton detection experiments were performed using the TL2 probe on the AS:PA100 sample and results are explored in Chapter 4.1. These four include the HNCO, HNCA, and HN(CO)CA experiments adapted from non-gradient solution NMR sequences described in reference 84; with the CBCA(CO)NH experiment adapted from reference 85. The adapted pulse programs for each are illustrated in **Figure 3.1**.

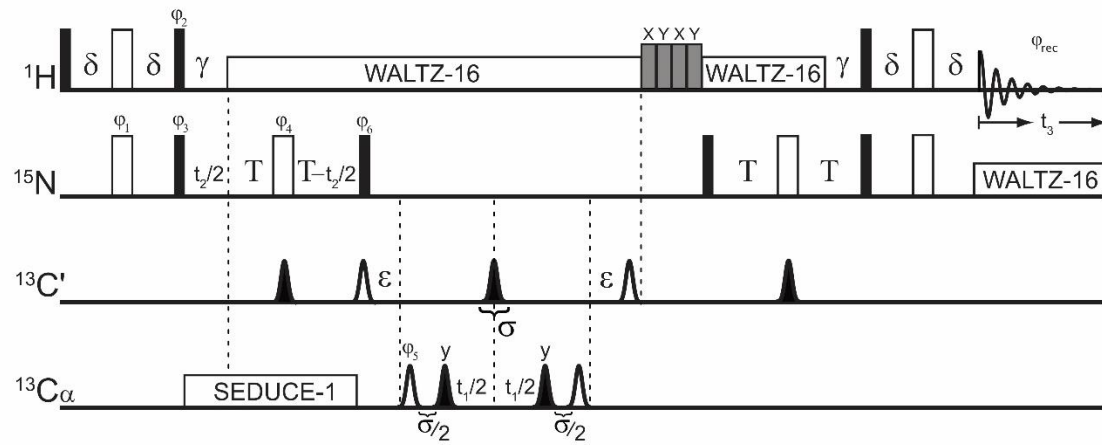
The hard proton, carbon and nitrogen 90° pulses were 3.75 μs , 5 μs and 7 μs , respectively. The associated the proton and nitrogen channel WALTZ-16 decoupling⁸⁷ were set to 10 kHz. Water suppression was achieved using the MISSISSIPPI sequence⁸⁶ applied for 200 ms at a power level corresponding to a B_1 field of 15 kHz. We utilize the SEDUCE-1 selective decoupling sequence for effective decoupling of ^{13}CO and $^{13}\text{C}^\alpha$ spins. These selective pulses utilize the WALTZ-16 phase cycle, effectively replacing the original WALTZ-16 pulses with carbon selective SEDUCE-1 pulses.⁸⁸ Multiple selective gaussian cascade shaped soft pulses of length σ at 400 μs on the carbon channels were utilized for refocusing and compensating for the Bloch-

Siegert phase effects.⁶¹ These are adapted into the pulse sequence and adjusted for where necessary, labelled by the associated σ delays. For example, within the HNCO/HNCA sequence in Figure 3.1, where the σ delay is introduced on the third channel, corresponding to the length of the selective pulse within the t_1 evolution period. The HNCA and HNCO experiments shared delays, including δ , γ and T at 2.5, 5 and 12.3 ms respectively. The HN(CO)CA experiment specific delay ϵ corresponded to 8.33 ms. The CBCA(CO)NH experiment delays include λ , κ , T, ϵ , ω , θ , T_N , γ and δ at 1.77, 2.2, 3.3, 3.3, 4.5, 11.4, 11.1, 5, and 2.5 ms, respectively.

HNCO / HNCA



HN(CO)CA



CBCA(CO)NH

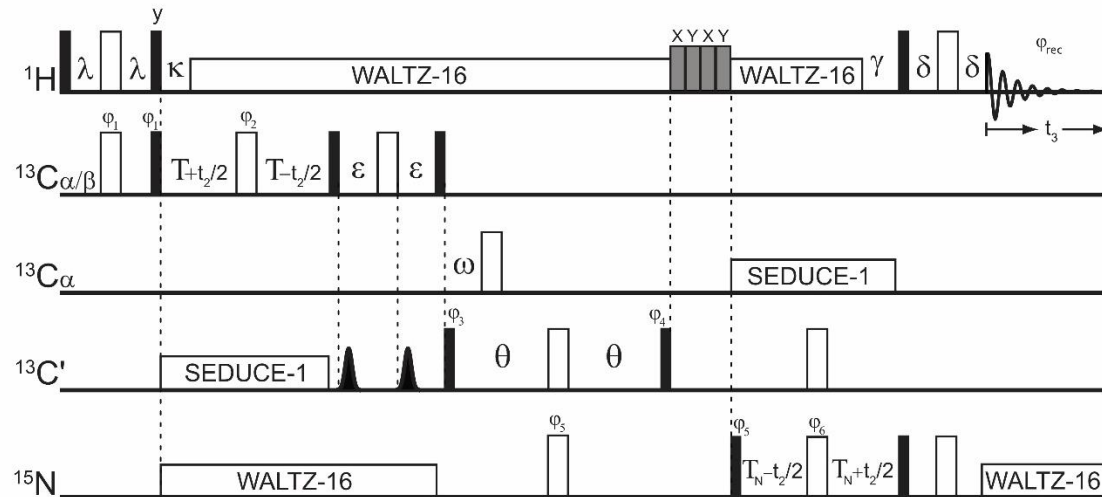


Figure 3.1 – Pulse programs for each 3D proton detection experiment. Black and white bars represent 90° and 180° pulses, respectively. Grey bars represent water suppression sequences while curved peaks represent shaped pulses. The HNCO and HNCA experiments had similar phase cycling: $\phi 1=y,-y$; $2=x,-x$; $\phi 3=2(x),2(x)$; $\phi 4=x$; $\phi 5=4(x),4(y),4(-x),4(-y)$; receiver= $2(x),4(-x),2(x)$. Quadrature detection was achieved using States-TPPI on $\phi 3$, $\phi 4$ and receiver. The phase cycle for the HN(CO)CA experiment was as follows: $\phi 1=x,-x$; $\phi 2=y,-y$; $\phi 3=x$; $\phi 4=4(x),4(y),4(-x),4(-y)$; $\phi 5=2(x),2(-x)$; $\phi 6=x,-x$; receiver= $2(x),4(-x),2(x)$. Quadrature detection was achieved using States-TPPI on $\phi 5$, $\phi 3$ and receiver. The phase cycle for the CBCA(CO)NH experiment was $\phi 1=x,-x$; $\phi 2=8(x),8(y),8(-x),8(-y)$; $\phi 3=4(x),4(-x)$; $\phi 4=x$; $\phi 5=2(x),2(-x)$; $\phi 6=8(x),8(-x)$; receiver= $x,2(-x),x,-x,2(x),2(-x),2(x),-x,x,2(-x),x$.

3.3.2 ¹³C detected NMR experiments

2D ¹³C-¹³C through-space correlation spectra using ¹H-¹³C CP for excitation and DARR mixing of 30 ms, 2D NCA through-space correlation spectra using ¹H-¹⁵N CP for excitation and ¹⁵N-¹³C CP for mixing, and 2D ¹³C-¹³C through-bond correlation spectra with ¹H-¹³C INEPT (Insensitive Nuclei Enhanced by Polarization Transfer)⁷⁵ for excitation and Total Through-Bond Correlation Spectroscopy (TOBSY)⁷⁶ of 7.133 ms mixing were recorded for all samples. All 2D ¹³C-¹³C spectra were processed in Bruker Topspin 4.0.6 with Lorentzian-to-Gaussian apodization function (using 20 Hz of Lorentzian line narrowing and a GB of 0.07) for the CP DARR 2D ¹³C-¹³C correlation spectra and squared cosine function for the INEPT TOBSY 2D ¹³C-¹³C correlation spectra and for all 3D correlation spectra.

Spectroscopic assignments were carried out on fibril samples using a suite of 3D CANCO, NCACB, NCACO, NCACX, NCOCA, NCOCX experiments, explored in Chapter 4.2. Band-selective versions of the SPECIFIC CP⁷³ was used for NCA or NCO transfers. Radio-frequency Driven Recoupling (RFDR)⁹⁰ with mixing time of 1.68 ms was used in the NCOCA/NCACO experiments; Dipolar Recoupling Enhanced by Amplitude Modulation (DREAM)⁹¹ mixing of 5 ms was used in the NCACB experiment. 3D NCACX and NCOCX experiments were recorded using Dipolar Assisted Rotational Resonance (DARR)^{92,93} recoupling with mixing times of 50 ms and 80 ms, respectively.

3.4 Chemical shift assignment methods

3.4.1 Through-bond multidimensional NMR correlation methods for characterization of mobile protein fragments.

Through the utilization of multiple 3D heteronuclear chemical shift correlation experiments, unambiguous ¹H, ¹³C, and ¹⁵N backbone and side chain chemical shift assignments of the mobile regions of a protein can be determined using proton detected experiments.^{19,96} Again, as internal motions within a protein are strongly anisotropic, MAS is required to achieve high spectral resolution and sufficiently long coherence lifetimes, necessary for chemical shift assignments techniques. The required experiments previously outlined include the INEPT based HNCA, HN(CO)CA, HNCO and CBCA(CO)NH (**Figure 3.1A**). The process involves linking and assigning spin systems to their associated amino acid type and subsequently mapping these systems to the protein sequence.

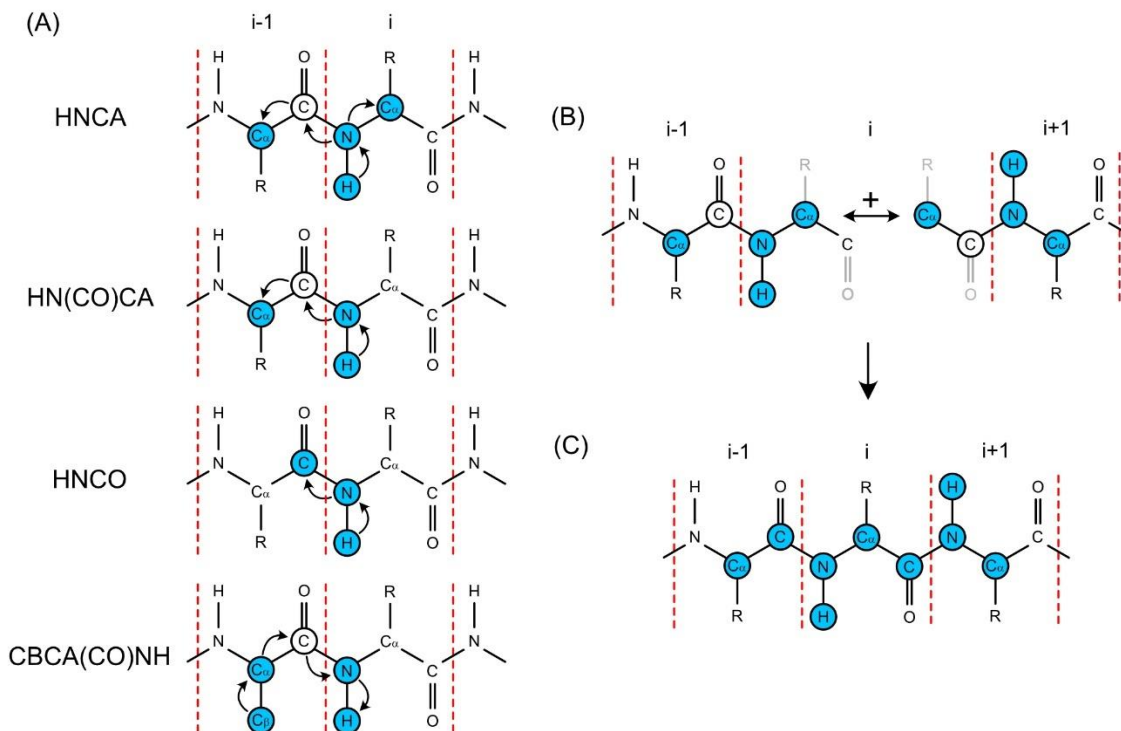


Figure 3.2 - (A) Schematic representation of the four experiments required for backbone chemical shift assignment of mobile protein fragments with their respective polarization transfer pathways and (B) a schematic representation of two neighboring systems being linked given distinguishable CA[i] and CA[i-1] shifts via HN(CO)CA, creating an extended spin system (C) with associated CO shifts via the HNCO experiment.

Spin systems are initially picked in the 3D HNCA spectrum with associated one-bond H[i]-N[i]-CA[i] and two-bond H[i]-N[i]-CA[i-1] correlations, linking two CA shifts to a single N[i]/H[i] chemical shift pair corresponding to the i^{th} spin system. The 3D HN(CO)CA experiment involves only the H[i]-N[i]-CA[i-1] correlation via an intermediate polarization transfer through CO[i-1], allowing for the discrimination between CA[i] and

CA[i-1] in the 3D HNCA. This distinction allows for neighboring spin systems [i] and [i-1] to be linked by matching the CA shifts shared between them as illustrated in **Figure 3.1B**, to form an extended spin system (**Figure 3.1C**). The CA[i] shift from system [i] has a matching CA[i-1] from the following system [i+1] within the HNCA spectrum. Matching of the H[i]/N[i] shift pair to the corresponding CO[i-1] shift can be accomplished via the 3D HNCO experiment which correlates H[i], N[i] and CO[i-1] atoms. Due to the lack of an amide proton, proline residues are not visible by HNCA or HNCO experiments and therefore cause interruptions in the linkage of spin-systems in the HNCA spectrum.

Once spin systems have been linked, amino-acid types are assigned largely based on their associated chemical shifts. For this purpose, the 3D heteronuclear INEPT based CBCA(CO)NH experiment is employed to gather CB shifts of each spin system for assignment of amino-acid types via CB[i-1]-CA[i-1]-N[i]-H[i] correlations (**Figure 3.1A**). Glycines lack a CB carbon, but can be identified through their unique CA chemical shifts, falling between 40-50 ppm. Alanines, serines and threonines can be assigned based on their unique CA/CB shift pairings. There is still remaining ambiguity in identifying the type of the remaining amino acids based on their overlapping CA/CB shifts. However, linking all possible spin systems and subsequent unambiguous identification of the unique amino acids is generally sufficient for sequence matching, achieving site specific chemical shift assignments.

3.4.2 Through-space multidimensional NMR correlation methods for characterization of rigid protein fragments.

Chemical shift assignments of the rigid protein fragments can also be obtained from 3D chemical shift correlation experiments. Multiple experiments must be utilized, and given good signal to noise and resolution, the NCACX, NCOCX and CANCO experiments provide the correlations required for a full backbone assignment (**Figure 3.2A**).^{58,97} However, under lower resolution and/or signal to noise conditions, experiments utilizing carbon specific polarization transfers can be used, directly correlating either the CA, CO, or CB shifts. In doing so, the transferred polarization is optimized, thereby maximizing the signal to noise in comparison to the non-specific CX polarization transfer. Nuclei specific experiments utilized in this thesis are the NCACO, NCACB, and NCOCA, which provide correlations normally visible in optimal NCACX and NCOCX spectra.

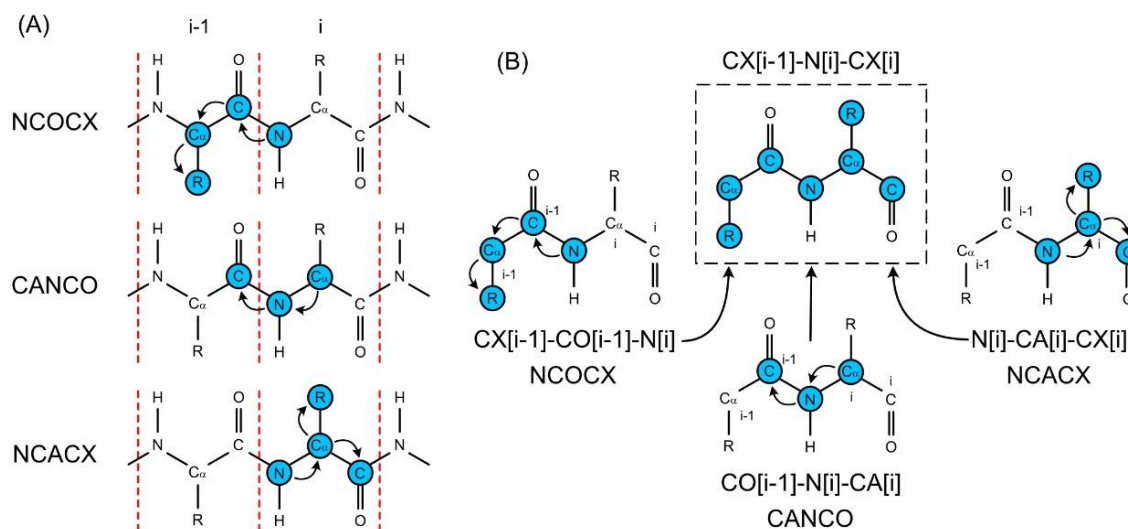


Figure 3.3 - (A) Schematic representation of the three experiments required for backbone chemical shift assignment of rigid protein fragments with their respective polarization transfer pathways and (B) a schematic representation of the formation of an extended spin system via correlated NCOCX and NCACX with the intervening CANCO.

The simple method for chemical shift assignments of rigid protein fragments for rigid protein fragments given sufficient resolution in the three NCOCX, NCACX and CANCO experiments is shown in **Figure 3.2B**. Systems are typically picked in the NCACX spectra, providing shift values for N, CA and interresidue CX shifts (CB, CG, etc.) for the i^{th} spin system $CX[i-1]-N[i]-CX[i]$. The CO shift of the preceding residue can be obtained via the CANCO experiment that correlates $CA[i]$, $N[i]$ and $CO[i-1]$ shifts. The backbone CA and CX shifts of the preceding residue can then be obtained via the NCOCX spectra, through the one-bond $N[i]-CO[i-1]-CA[i-1]$ and two-bond or longer $N[i]-$

CO[i-1]-CX[i-1]. These extended spin systems can then be linked by matching the CX (CO, CA, CB, etc.) shifts between the NCACX and NCOCX spectra and, finally, mapped to the protein sequence. With this, nearly the entirety of a protein can be assigned, save for fragments with intermediate dynamic properties, preventing their detection in either through-bond or through space experiments. In the case of α -syn, once chemical shifts are obtained for the monomeric lipid-bound and fibril forms, thereby verifying their structural characterizations, conformational changes induced in fibrils via lipid-binding can be traced site-specifically.

4 Results and Discussion

To characterize the refolding effect of anionic lipids on fibril structure upon interaction, we contrasted samples containing either 1) monomeric α -syn bound to anionic lipid containing vesicles, 2) fibrils alone, or 3) fibrils bound to anionic lipid containing vesicles using solid state nuclear magnetic resonance (ssNMR). This lipid system was enriched in CL in order to mimic the OMM under stress conditions. To evaluate if effects were CL-specific (that is, driven by specific interactions between CL and α -syn) or more simply related to electrostatic interactions between the CL charged headgroups and charged residues of α -syn, we also monitored the conformation of α -syn fibrils in the presence of complementary liposomes containing a similarly charged anionic lipid that is enriched in mitochondrial membranes, phosphatidic acid (PA). We utilize NMR strategies outlined in Chapter 3.4 to conduct chemical shift assignments of the membrane-bound monomeric α -syn and fibrils to site-specifically track changes between the intact fibril and its lipid-bound state. We begin with the mobile C-terminal tail of the lipid-bound conformation and the extension of these shifts to the fibril form (Chapter 4.1), before assigning the rigid fibril core (Chapter 4.2.1).

We show that Interactions with TOCL or DOPA containing vesicles have similar effects on fibrils. Helical content is indeed induced, and the fibril core, while retaining most of the original β -structure, is clearly perturbed and partially destabilized. Tracking the conformational differences induced by lipid interactions and comparing results to published structures and other data, we propose that N-terminal lipid binding is likely

induced, resulting in conformational changes within the core in addition to a motionally restricted or interacting C-terminal tail.

4.1 Resonance assignments of the flexible regions of monomeric α -synuclein: conformation of C-terminus in the lipid-bound and amyloid fibril states

This chapter has been republished (in part):⁷⁹

Medeiros, J.; Bamm, V. V.; Jany, C.; Coackley, C.; Ward, M. E.; Harauz, G.; Ryan, S. D.; Ladizhansky, V. Partial Magic Angle Spinning NMR ¹H, ¹³C, ¹⁵N Resonance Assignments of the Flexible Regions of a Monomeric Alpha-Synuclein: Conformation of C-Terminus in the Lipid-Bound and Amyloid Fibril States. *Biomol. NMR Assign.* **2021**.

It is republished with permission from Springer Nature. The full text is available at <https://link.springer.com/article/10.1007%2Fs12104-021-10020-z>. Further permissions related to the material excerpted should be directed to Springer Nature.

4.1.1 Assignments and data deposition

As was discussed in Chapter 1, α -syn is intrinsically disordered in the soluble state,^{98–100} and numerous previous investigations suggest the presence of flexible domains within the lipid- or detergent-bound protein^{23,30,101} as well as in the fibrillar

form.^{102,103} Previous reports have shown that localized motions of sufficient amplitude combined with MAS enable proton detection in globally immobilized proteins,^{94,96,104,105} provided that the motions are sufficient to lead to long transverse relaxation times for successful INEPT polarization transfer steps. To examine mobility of α -syn in the lipid bound and fibrillar states, 2D ^{13}C - ^{13}C INEPT TOBSY correlation spectroscopy was carried out on all three samples (AS:CL100, AS:PA100 and fibrils). A comparison of the 2D spectra of AS:PA100 and AS:CL100 samples is shown in **Figure 4.1A**. Largely similar cross peak patterns indicate that conformations of the flexible regions of α -syn in these samples are similar, although the cross peaks are more intense and narrower in the AS:PA100 sample, suggesting a higher degree of mobility. In contrast, fewer and significantly less intense peaks are observed in the 2D carbon-carbon correlation spectra of α -syn fibrils (**Figure 4.1B**), indicating that while most of the same residues remain flexible in the fibrillar form, they are more dynamically restrained.

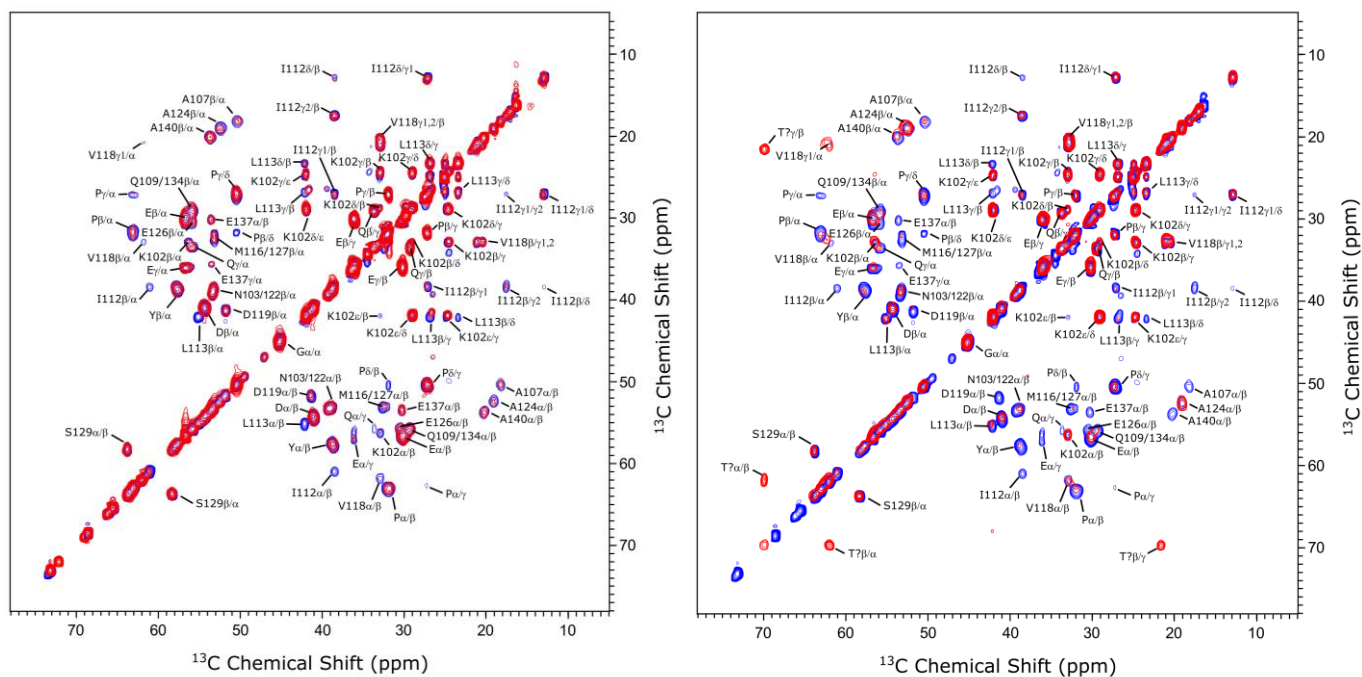


Figure 4.1 - A comparison of 2D INEPT TOBSY carbon-carbon correlation spectra collected on (A) AS:PA100 (blue) and AS:CL100 (red) samples, and on (B) AS:PA100 (blue) and fibril (red) samples.

To obtain *de novo* assignments and site-specifically identify the regions that remain mobile, we carried out chemical shift assignments on the AS:PA100 sample as this sample had the most favorable relaxation properties. A suite of four 3D correlation experiments, HNCO, HNCA, HN(CO)CA and CBCA(CO)NH was recorded. Typical amide proton line widths of well-resolved peaks were 0.1 ppm and were comparable to those detected in mobile fragments of other membrane bound and fibrillar systems.^{94,96,104} A total of 60 resolved intra- and inter-residue cross peaks were detected in the least sensitive backbone correlation HNCA experiment, in addition to

several overlapping peaks due to glutamates. These were complemented with 34 non-prolyl inter-residue correlations in the HN(CO)CA experiment. Both sensitivity and resolution were sufficient to reliably detect sidechain CB resonances and identify the amino acid types in the CBCA(CO)NH experiment. These experiments were analyzed together to perform a backbone walk, an example of which is shown in **Figure 4.2** for residues G132-E137. A total of 40 residues, all located in the C-terminus (101-140), could be assigned from the 3D experiments. Furthermore, a comparison of the CA and CB chemical shifts detected in the 3D CBCA(CO)NH and in the 2D ^{13}C - ^{13}C INEPT-TOBSY spectra further allowed us to extend assignments to more distal aliphatic side chain carbon atoms as illustrated in **Figure 4.3** and summarized in **Table A1**. The detected backbone chemical shifts indicate that the C-terminus is unstructured when bound to DOPA:DOPC lipid vesicles (**Figure 4.4**), in agreement with previous solution and solid-state NMR data.^{23,30} The chemical shift assignments were deposited to BioMagResBank (<http://www.bmrb.wisc.edu>) under BMRB entry 50746.

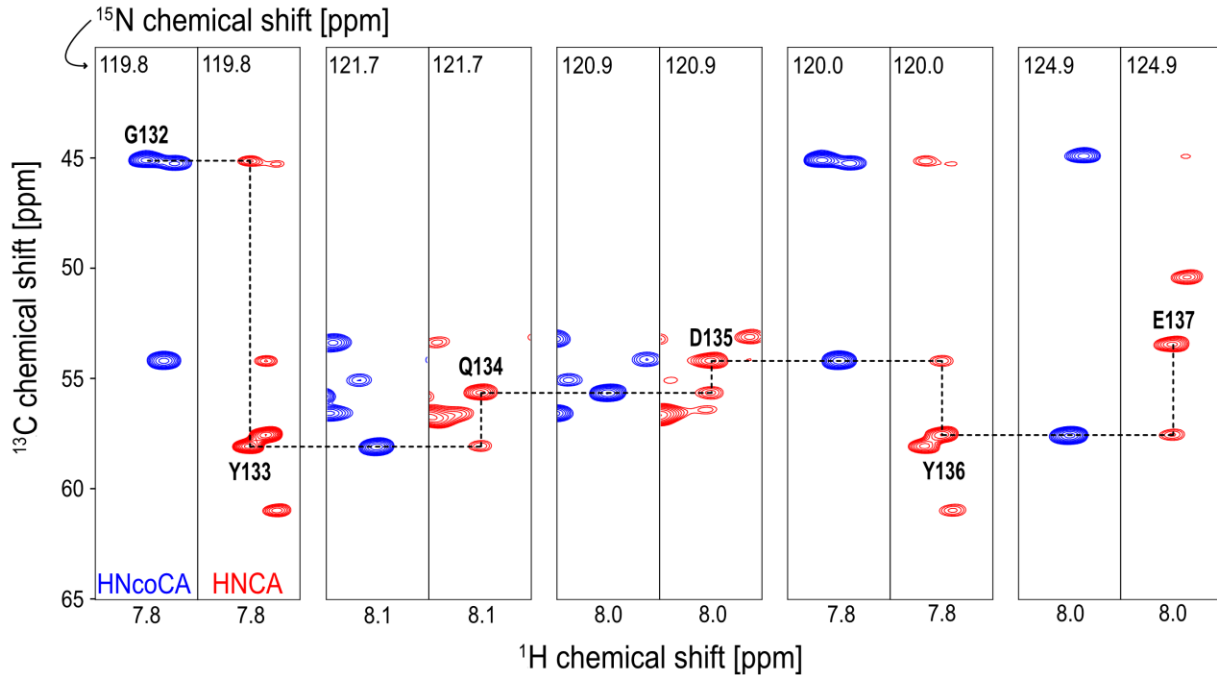


Figure 4.2 - Backbone assignment walk using HNCA (red) and HN(CO)CA (blue) experiments for residues G132-E137 on a AS:PA100 sample.

Although proton detected 2D HSQC spectra could be measured in the AS:CL100 sample, the relaxation properties were not sufficiently favorable for heteronuclear 3D experiments which require long INEPT transfer steps. However, a direct comparison of the 2D ^{13}C - ^{13}C INEPT-TOBSY spectra recorded on the AS:PA100 and AS:CL100 samples (**Figure 4.1A**) indicates similar conformation of the C-terminus in both lipid-bound forms and also allows for selected assignments of resolved cross peaks due to backbone and side chain carbons (**Table A1**).

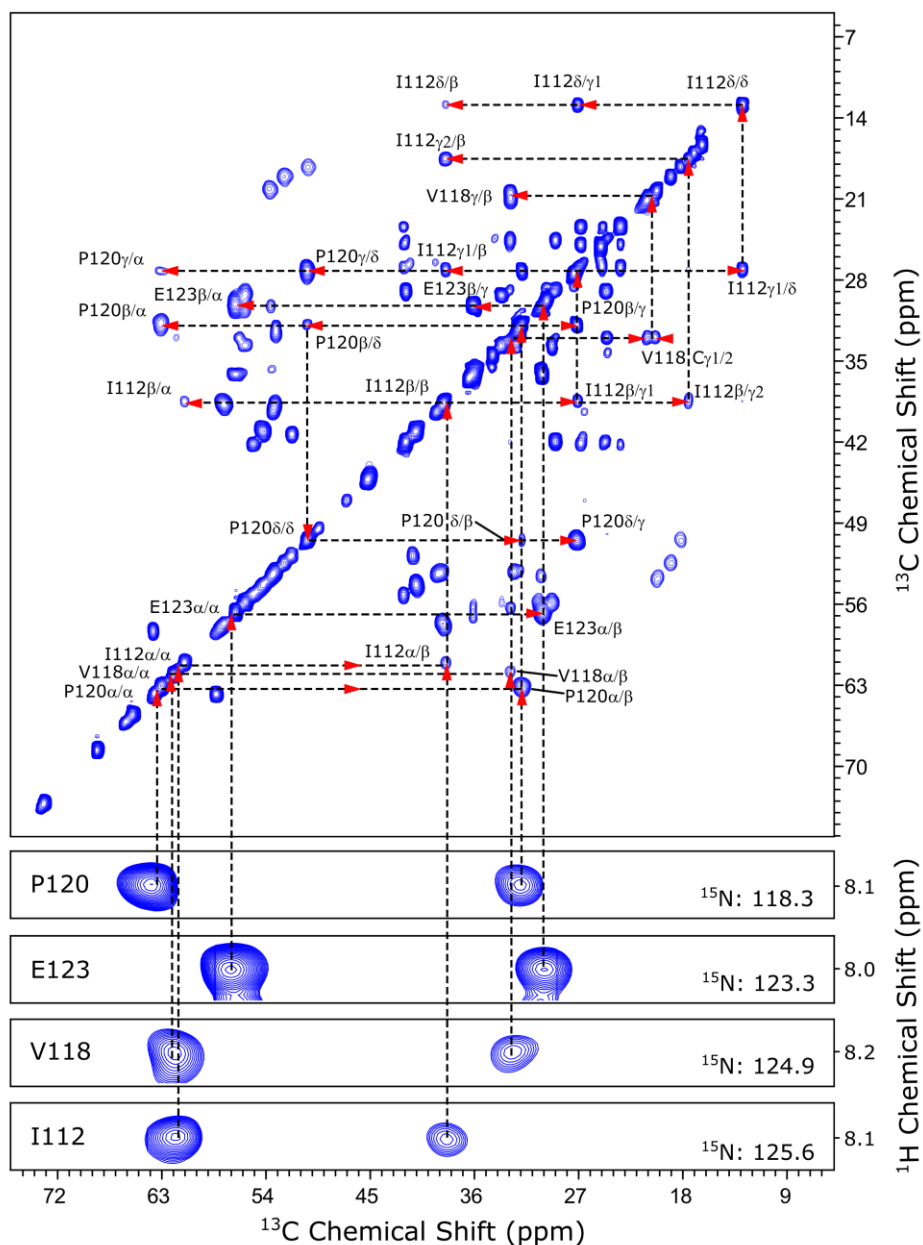


Figure 4.3 - Assignments of side chain resonances using 3D CBCA(CO)NH and 2D ^{13}C - ^{13}C INEPT TOBSY correlation spectra collected on AS:PA100 sample. CB and CA resonances were matched in the two experiments, were further extended to additional side chain carbon resonances as illustrated for I112, V118, P120 and E123.

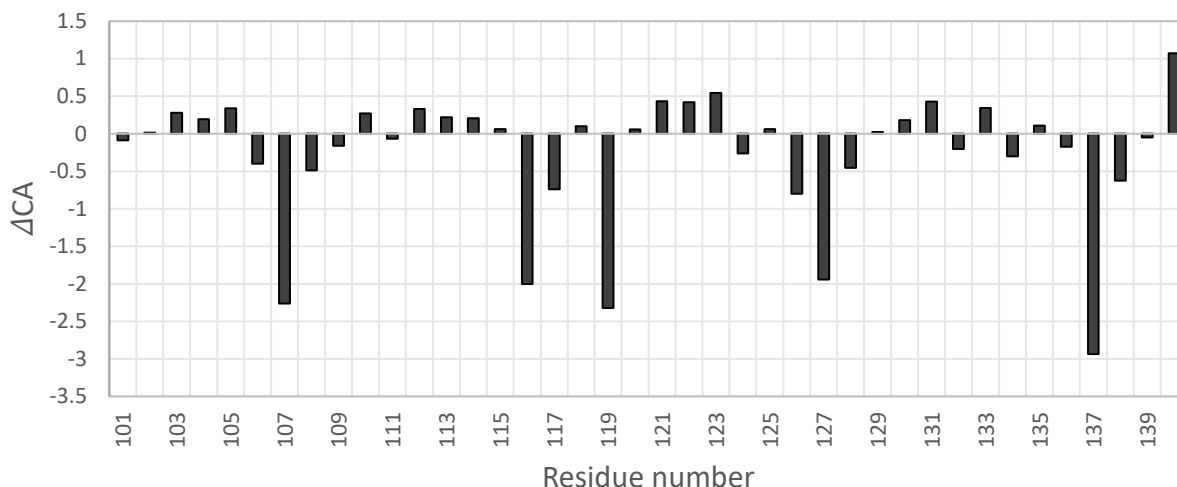


Figure 4.4 - Secondary $^{13}\text{C}\alpha$ shifts of sequentially assigned residues in the C-terminus of α -syn bound to DOPA:DOPC LUVs. Values for average chemical shifts corresponding to random coil were taken from ¹⁰⁶.

Significantly attenuated cross peak intensities in the 2D ^{13}C - ^{13}C INEPT-TOBSY spectra of the fibrils indicate even more restrained dynamics, however, the cross-peaks detectable in the C-terminus had nearly identical chemical shifts to those in the AS:PA100 sample (**Figure 4.1B**). These correspond to eight residues that span the entire C-terminus thus suggesting that the terminus is unstructured and flexible, in general agreement with previous findings.^{102,103} Chemical shift assignments obtained by chemical shift mapping for overlapping resonances are given in **Table A3**. Interestingly, in addition to the C-terminus signals, the 2D ^{13}C - ^{13}C INEPT-TOBSY spectrum of the fibrillar sample had a unique threonine cross peak at 61.9/69.9 ppm (CA/CB) and 69.9/21.6 ppm (CB/CG). The *in vitro* structure of α -syn fibrils is very sensitive to even

small variations in fibrillization conditions. Multiple polymorphs have been characterized to a different degree using solid-state NMR chemical shifts^{40,102,103,107,108} and structural determination,²⁴ as well as by cryo-electron microscopy.^{51,109,110} There is general agreement on the existence of the rigid β -structured core comprising residues *ca.* 38-100, but conformations of the termini vary between polymorphs. The threonine cross peak detected in the 2D ^{13}C - ^{13}C INEPT-TOBSY spectrum is in agreement with random coil values.¹⁰⁶ This peak corresponds to a residue outside the C-tail given its lack of threonine, and likely results from flexible and disordered domains in the N-terminus.

In summary, we took advantage of the high degree of flexibility of the C-terminus of α -syn bound to DOPA:DOPC lipid vesicles, and used MAS 3D chemical shift correlation spectroscopy to determine chemical shifts and characterize its conformation. The C-terminus was found to be more motionally restricted, yet mobile, in the α -syn bound to TOCL:DOPC lipid vesicles mimicking mitochondrial membranes under stress, and in the α -syn fibrils. With these assignments in hand for later analysis, we move to determining the chemical shift assignments for rigid residues in the fibril core, as these will likely undergo the largest conformational changes following refolding due to lipid-interactions.

4.2 Interaction of α -synuclein fibrils with lipids

4.2.1 Chemical shift assignments of α -synuclein fibrils

Similar to other fibril-forming proteins, α -syn can form structurally distinct polymorphs, depending on the conditions used to initiate fibrillization. Several *in vitro* α -syn polymorphs have been reported in the literature and characterized structurally, including by NMR.^{17,41,42,43,44,45,46} Based on the comparison of chemical shift correlation spectra, the α -syn fibrils used in this study are distinct from those previously published. To characterize conformational transitions in fibrils induced by interactions with anionic lipids at atomic level, spectroscopic assignments utilizing three-dimensional (3D) CANCO, NCACX, NCOCX, NCACB, NCACO, NCOCA correlation experiments were carried out as described previously.^{111,97} A total of 60 resolved inter-residue cross-peaks corresponding to 60 residues in the rigid fibril core, and a degenerate overlapped multi-peak correlation were detected in the CANCO spectrum. Of these, a total of 28 residues were assigned unambiguously. Spectral overlap caused by a large population of similar residues within repeat regions, local structural heterogeneity, as well as insufficient signal to noise have prevented further unambiguous assignments. All assigned residues were either found in the vicinity of the NAC domain, e.g., G41-S42, G51-A56, or within the NAC domain itself, e.g., G68-V71, G73-K80, and E83-A90, and their chemical shifts indicate the expected β -structure (**Figures 4.6** and **4.7**). An example representative of the backbone walk for residues G86-A90 is shown in **Figure 4.5**. Assignments are reported in appendix Table **A2.1**.

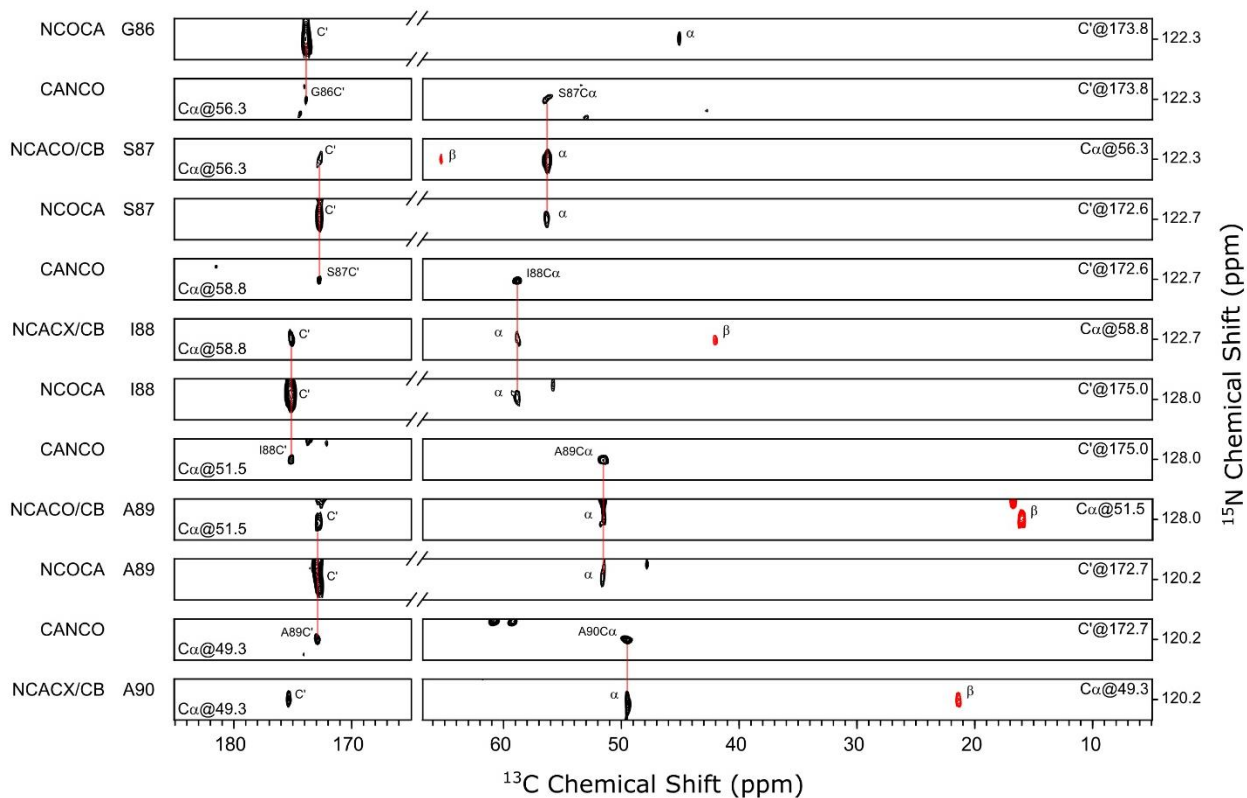


Figure 4.5 - A representative backbone walk for residues G86-A90 obtained using a suite of 3D heteronuclear experiments indicated on the left for each strip. Strips with multiple experiments labelled indicate an overlay, for example, NCACO/CB indicates the overlay of both corresponding NCACO and NCACB strips. Cross peaks with negative intensities obtained in the NCACB experiments with DREAM mixing are shown in red.

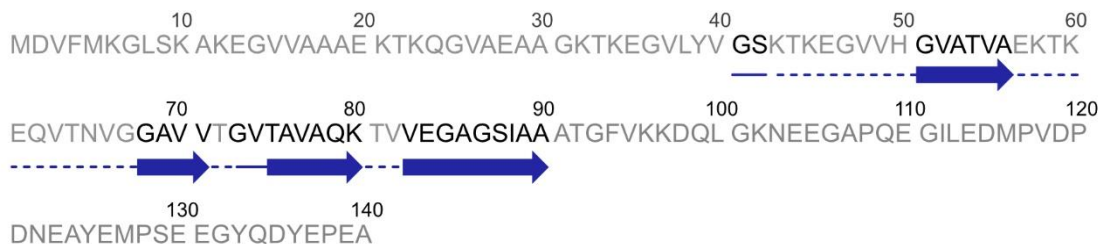


Figure 4.6 - Amino acid sequence of α -syn, with residues assigned shown in bold and secondary structure indicated below (based on CSI values reported in Figure 4.7), and dashed lines indicate unassigned residues (grayed) connecting assigned portions.

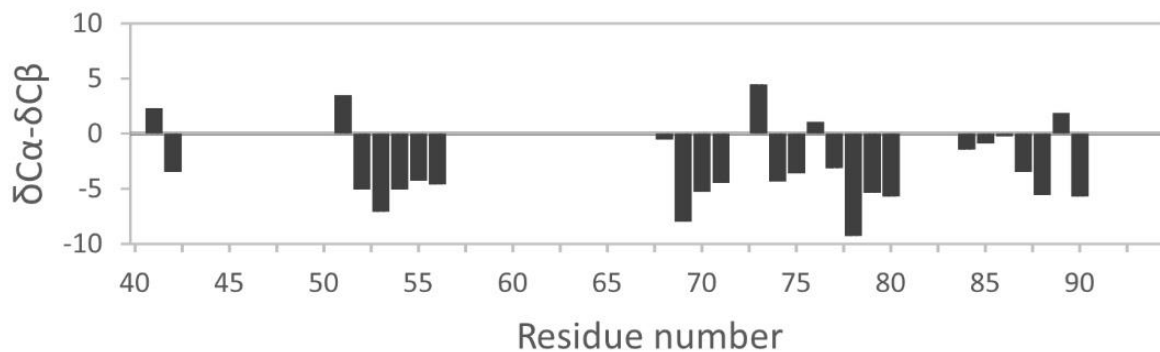


Figure 4.7 - Chemical Shift Index (CSI)¹¹² for assigned residues in α -syn fibrils. Random coil values were taken from reference 78.

4.2.2 Interactions of fibrils with anionic lipids induce changes in the fibril core

To characterize conformational changes in α -syn fibrils upon interaction with anionic lipids, fibrils were exposed to liposomes containing TOCL lipids mimicking the OMM under stress. Previous circular dichroism (CD) studies of interactions of α -syn fibrils with lipid membranes at a PLR of 1:300 containing 30% TOCL (as well as other charged lipids, equating to a surface charge equivalent to that of the LUVs used in this study) showed a decrease in β -structure of ~40%, suggesting that interactions with TOCL result in the restructuring of fibrils.¹⁹ However, these studies were not able to inform on the conformational changes at an atomic level.

Here, we employ 2D ssNMR to detect site-specific chemical shifts to examine the conformation of the lipid-bound fibrils and to contrast it with conformations of α -syn in intact fibrils, as well with monomeric α -syn bound to TOCL-containing lipid vesicles. Chemical shifts of nuclear spins in the protein backbone and sidechains are exquisitely sensitive to the local structure and chemical environment and can be used to characterize conformational transitions. In addition, to evaluate if the effects were CL-specific or related to electrostatic interactions, we also monitored the conformation of α -syn fibrils in the presence of liposomes containing another anionic lipid DOPA, chosen for its similar net charge to TOCL at neutral pH, and known localization to mitochondrial membranes.¹¹³ α -syn in the lipid-bound or fibrillar forms has been shown to exhibit differential mobility across its three domains (N-terminus, NAC, and C-terminus), the mobile fragments of which were compared in Chapter 4.1.^{22,26,27,114–116} Here, we employ

through-space and through-bond spectroscopies to visualize motion restricted and mobile fragments of α -syn.

Through-space 2D CP DARR ^{13}C - ^{13}C correlation spectra with mixing times of 30 ms were recorded on all samples to establish primarily intraresidue correlations (**Figure 4.8**). These spectra are expected to yield the structural signatures of the N-terminal domain (residues 1-60) and NAC domain (residues 61-98) that are expected to be relatively rigid in both fibrillar and monomeric lipid-bound states.^{23,99,101,117–120} Several amino acid specific regions corresponding to CA/CB correlations from alanines, serines and threonines, and CB/CG correlations from threonines, all of which are preferentially present in the first 100 residues of α -syn (10/10 threonines, 3/4 serines and 16/19 alanines), can be used to track conformational transitions within fibrils induced by interactions with lipids.

The 2D DARR ^{13}C - ^{13}C spectrum of fibrils indicates the expected β -content across all amino acid specific regions (**Figure 4.9**), in agreement with the CSI of assigned fibril chemical shifts (**Figure 4.7**). Analysis of spectral intensities suggests that nearly the entire N-terminus and the NAC domain are visible in the DARR spectrum of fibrils. Indeed, the Ala CA/CB correlation region contains several resolved peaks that can be used to gauge a single residue contribution to the spectral intensity. Using this approximate calibration, we estimate that the total intensity of the Ala CA/CB correlation corresponds to ~19 Ala (16 are expected to be in the rigid domains). A similar analysis of the threonine CB/CA correlation region suggests that ~10 Thr are visible in the through-space spectra of fibrils, matching the total number of threonines within the

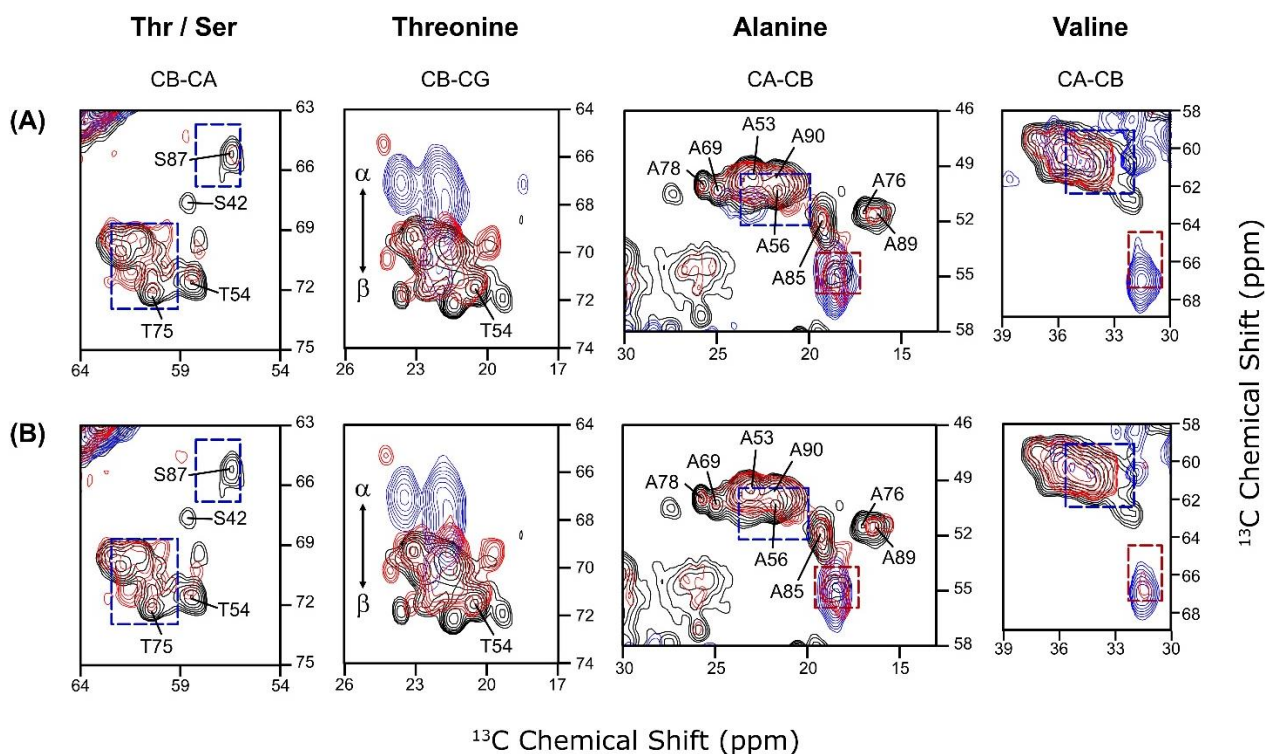


Figure 4.9 - Expanded amino acid specific regions of the 2D ^{13}C - ^{13}C CP DARR spectra of fibrils (black) and (A) F:CL300 (red) and AS:CL100 (blue) and (B) F:PA300 (red) and AS:PA100 (blue), including Thr & Ser CB/CA, Thr CB/CG, Val CA/CB, and Ala CA/CB. Dash bordered boxes indicate regions typical of β -structure (blue) and of α -helical structure (red) while the arrow within the Thr CB/CG region indicates structure propensity via the CB shift. The widths of the boxes correspond to one standard deviation from mean values as reported in reference 78.

Numerous solution and solid-state NMR studies of α -syn monomers bound to anionic lipids suggest that the N-terminal region of the protein adopts α -helical structure,^{14,26,27} albeit this region retains a significant degree of dynamics.¹¹⁸ Consistent with this, α -syn in both AS:CL100 and AS:PA100 samples show similar and predominantly helical structure, based on the similar distribution of chemical shifts,

which is especially evident in the Ala CA/CB correlation regions (**Figure 4.9**). Although Thr and Ser CA/CB correlations corresponding to α -helical regions are not resolved in the carbon-carbon correlation spectra as they may completely or partially overlap with the spectral diagonal, the CB/CG side chain correlations of threonines as well as of valines are distinct, and they clearly indicate α -helical structure (**Figure 4.9**). In agreement with this, the backbone threonine and valine correlations centered at 120/67.5 ppm in the 2D NCA spectra of the lipid-bound α -syn monomers also correspond to α -helical structure, although limited signal intensity in the case of AS:PA100 suggests greater mobility within the helical domain (**Figure 4.10**). Reduced CP excitation efficiency of both monomeric samples indicates their higher degree of mobility as compared to fibrils; of the two, α -syn is more mobile in AS:PA100, which is also consistent with the reduced signal-to-noise ratio (SNR) in the 2D NCA spectra.

The presence of spectral correlations due to the side chains of I88 in **Figure 4.8** suggests that it remains relatively rigid but non-helical as suggested by the CA/CB correlation at 58.1/41.1 ppm as well as multiple side chain correlations. There are only two isoleucines in the sequence of α -syn; the second (I112) is located in the C-terminus and is mobile as evident from strong Ile correlations in the 2D ^{13}C - ^{13}C INEPT TOBSY spectra (**Figure 4.1 & 4.11**). Comparatively, while several lipid-bound monomeric α -syn studies noted in Chapter 1 suggest helices reaching the start of the C-terminal tail, one study found the region of residues 26-97 to have intermediate dynamic properties which increase toward the C-terminus, suggesting transient mobility this far into the helix dependent on lipid composition.¹¹⁶

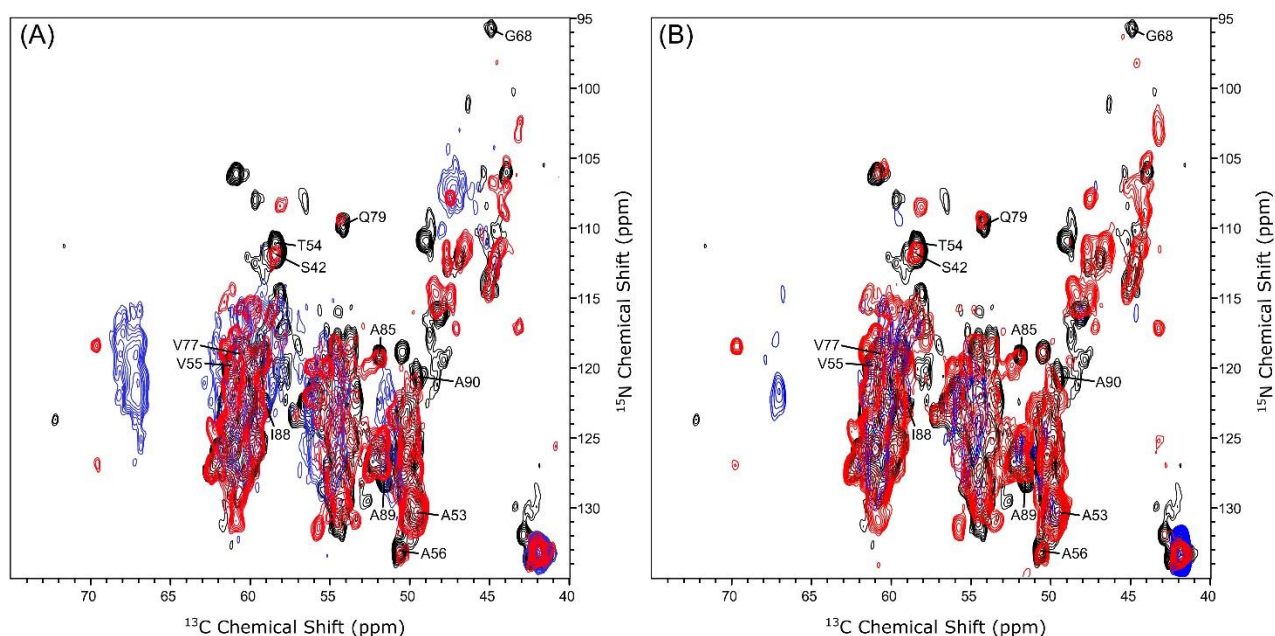


Figure 4.10 - Overlay of 2D NCA spectra of (A) fibrils (black), F:CL300 (red) and AS:CL100 (blue) and (B) fibrils (black), F:PA300 (red) and AS:PA100 (blue) showcasing several altered and new peaks via lipid interactions, while highlighting the helicity of the dynamic monomeric form via the Thr/Val correlations. The first contour is cut at 4.5σ , and subsequent contours are shown with a multiplication factor of 1.2. Selected assignments for several residues in fibrils are shown.

Interactions of fibrils with both TOCL and DOPA (samples F:CL300 and F:PA300) induce similar structural changes in α -syn, as evident from largely similar NMR spectra of F:CL300 and F:PA300 (**Figures 4.8, 4.10, 4.11**). The appearance of cross peaks corresponding to α -helical structure and more subtle changes in positions of many peaks within the β -structural regions in the 2D DARR correlation spectra suggest restructuring of fibrils (Thr CB/CA and CB/CG specifically). The presence of new α -helical structure is most evident in the Ala CA/CB correlation region (**Figure 4.9**)

in which there appears a clear spectral band at around 55.0/18.3 ppm, similar to that observed in the monomeric AS:CL100 and AS:PA100. This α -helical correlation accounts only for about 20% of the total Ala CA/CB integrated spectral intensity. Although no appearance of α -helical structure in the Thr CB/CA and Ser CA/CB correlation regions can be detected, and there is no appreciable intensity in the 2D NCA spectra around 120/67.5 ppm where Val/Thr α -helical correlations are expected (**Figure 4.10**), there is a uniform reduction of cross-peak intensities corresponding to β -structure in these regions as compared to intact fibrils. Together these data suggest that the β -strand to α -helical conversion involves a limited number of residues, while uniformly reducing the observable β -structure overall. The relatively increased mobility of the α -helical lipid-bound regions observed in the lipid-bound monomers may explain lack of α -helical correlations in the 2D ^{13}C - ^{13}C and NCA correlation spectra.

Changes in intensities and/or positions of the well-resolved peaks in the 2D ^{13}C - ^{13}C CP DARR spectra of fibrils upon their exposure to LUVs could be used to track lipid-induced conformational and dynamic changes in fibrils site-specifically. Although both 2D DARR and NCA correlation spectra of F:CL300 and F:PA300 samples have limited resolution, there are a total of 28 resolved peaks corresponding to 16 residues. Cross peaks with identical or nearly identical chemical shifts represent the conserved core of the fibrils that are not affected by lipids. These include N65CB/CA, G84C'/CA and A85 (NCA and CA/CB – with shifted CO) suggesting that the local regions surrounding these residues remain structurally similar to the original fibril core. There are several strongly attenuated or entirely missing cross peaks in the spectra of both F:CL300 and F:PA300

samples, representing structurally or dynamically perturbed domains (**Figures 4.8 & 4.9**) although several peaks remain unassigned. Similarly, multiple new and shifted peaks as well as peak attenuation are observed in the NCA spectra (e.g., S42, A53, T54, A56, G68, I88, A85, A89, A90) of F:CL300 and F:PA300 as compared to fibrils, suggesting a largely β -structured but perturbed conformation which is distinct from both the fibril and monomeric forms (**Figure 4.10**). Specifically, I88, A89 and A90 are entirely shifted and/or attenuated, while Q79 shifts only slightly and G68 completely disappears for both spectra, suggesting significant mobilization of these and possibly neighboring residues. Notably, the two CA/CB correlations from S42 and S87 are nearly completely attenuated in the 2D DARR spectra, and a new single contour serine peak at 64/58.5 ppm (stronger for F:PA300) is visible in **Figure 4.9**. In addition, T54 and T75 CB/CA are nearly completely attenuated. Interestingly, I88 CA/CB disappears in the 2D ^{13}C - ^{13}C correlation spectrum of F:CL300 and nearly so in the spectra of F:PA300. Its corresponding CB/CG2 intraresidue correlation remains but is clearly partially perturbed, splitting to a new and distinct isoleucine correlation, suggesting heterogeneity in the fibril form at this location.

Overall, increased α -helical content and a significant overall intensity attenuation of the 2D CP DARR spectra for F:CL300 and F:PA300 suggest reduced overall rigidity in the backbone of the fibril core. This could potentially indicate a destabilized fibril core or partial transition from β -sheet to helical structure or unbound monomer in solution, however the lack of many new peaks in the respective 2D INEPT spectra argues against the latter. All amino acid specific regions in **Figure 4.9** experience significant

attenuation, with an overall integrated intensity reduction of Ala CB/CA content to ~30% relative to the fibril form for both samples. Threonines and valines show a similar integrated intensity reduction of β -sheet content, and while the increase in helical CA/CB correlation intensities is observable, it is quite low in comparison to their respective monomeric forms as evident in **Figure 4.9**. The overall attenuation of signal in the 2D CP DARR spectra and disappearance of specific residues is suggestive of mobilized residues, necessitating the exploration of the mobile regimes of the restructured fibrils via through-bond correlation spectroscopy.

4.2.3 Interactions with lipids induce mobility within otherwise structured regions along with perturbations to the C-terminus of fibrils

2D ^{13}C - ^{13}C INEPT TOBSY through-bond correlation spectroscopy allows for visualization of the mobile fragments of α -syn, complementing the above DARR observations. As was explained in Section 4.1, nearly the entire C-terminus of the monomeric DOPA-bound α -syn has been assigned *de novo* (101-140), and many of these assignments could be transferred to the AS:CL100 and fibrils.⁷⁹ Compared to the spectra of AS:CL100, AS:PA100 and fibrils, 2D ^{13}C - ^{13}C INEPT TOBSY spectra collected on the F:CL300 and F:PA300 samples reveal additional correlations and several residues with perturbed chemical shifts relative to the fibril form. This indicates that the C-terminal fibril conformation is different from either the monomeric lipid-bound or fibrillar forms, and that there are additional resonances from either the N-terminus or

NAC domain that become mobilized upon the exposure of fibrils to lipids (**Figure 4.11**). Most notable are the presence of four cross peaks corresponding to serine CB/CA correlations. Of those, only one could previously be assigned to S129 in the C-terminus, while the other three resonances, although not assigned uniquely, likely correspond to the remaining three serines S9, S42, S87, or a heterogeneously shifted S129. This observation correlates with the attenuation of the S42 and S87 cross peaks in the 2D DARR spectra of F:CL300 and F:PA300 samples. Further supporting mobilization are four correlations corresponding to threonines, one of which remains consistent with the unassigned peak in the fibril spectra while the others represent completely new correlations. A single new potential intraresidue isoleucine or valine correlation at 25/16 ppm also indicates increased mobility in the N-terminus or NAC domains, potentially belonging to I88. Interestingly, clear alterations of the assigned C-terminal correlations are observed, including a significant shift in sidechain signals of I112 and neighboring L113, in addition to large proline and tyrosine shifts. Overall, perturbations of the C-terminal tail indicate a significantly altered and motion restricted tail, while new correlations suggest increasingly mobile N-terminal and NAC residues. The lack of other unique backbone correlations expected given the large attenuation of signal in the 2D CP DARR spectra suggests the altered fibril form retains some rigidity.

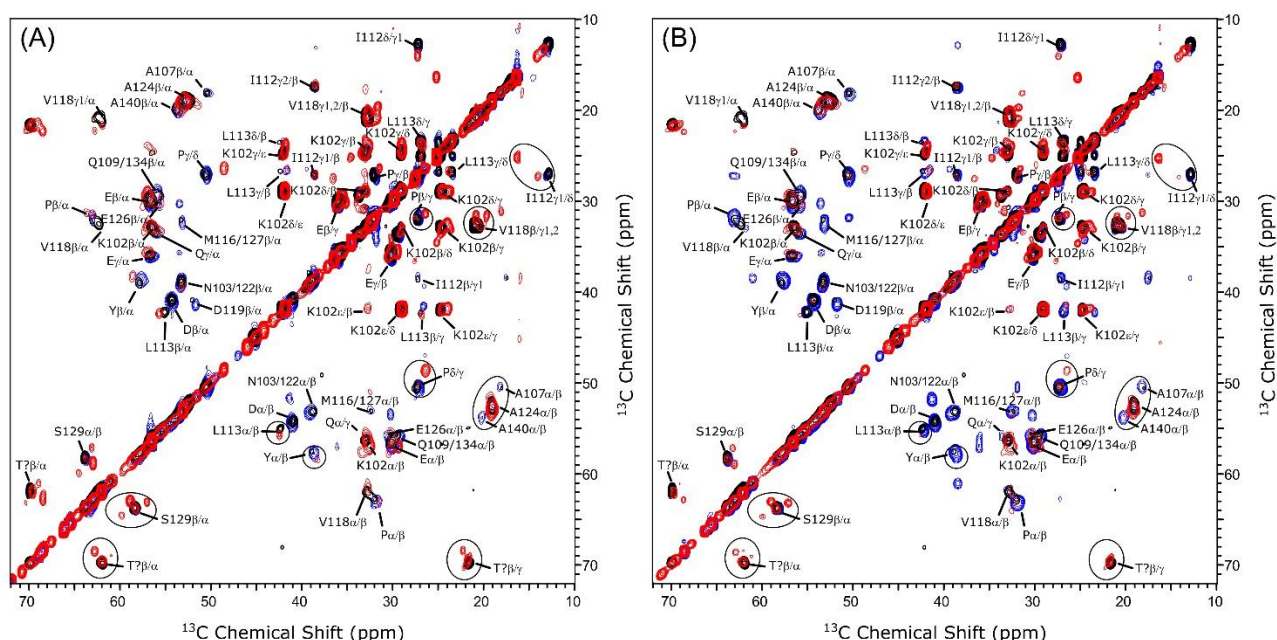


Figure 4.11 - Overlay of 2D ^{13}C - ^{13}C INEPT TOBSY spectra of (A) fibrils (black), F:CL300 (red) and AS:CL300 (blue) and (B) fibrils (black), F:PA300 (red) and AS:PA300 (blue). Regions or perturbations of note are circled. Transferable assignments from AS:PA100 to F:CL300 & F:PA300 include K102 (all correlations), I112 (β , γ 1/2), L113 (with shifted $\text{C}\alpha$ of just over 1 ppm), V118 (with attenuated α/β), A124, A140 (with attenuated α/β) and S129. The first contour is cut at 4.7σ , and subsequent contours are shown with a multiplication factor of 1.4.

4.2.4 Discussion

In addition to the C-terminus study discussed in Chapter 4.1, monomeric α -syn bound to both TOCL and DOPA containing LUVs showcase similar helical content extending at least to the observable I88, consistent with previously published data as previously noted. Although, the different lipid compositions do result in differences of observed mobility, with α -syn monomers being more rigid in the presence of CL

containing LUVs, reflected both in the observations of the helical region and C-terminal tail.

Our measurements suggest that DOPA and TOCL anionic lipids perturb fibrils in a similar way, given that both DOPA and TOCL containing LUVs result in very similar chemical shift perturbations of the fibril core and C-terminus. β -sheet structure indicative of the original fibril form was observed for both TOCL and DOPA containing samples, suggesting the conservation of these specific regions of the fibril core after lipid exposure. The lower bound estimate on the amount of helical structure induced in both samples (F:CL300 & F:PA300) amount to a minimum of ~20%; in comparison, previously published CD results are fairly consistent with 40% α -helical content.¹⁹ The discrepancy may be due to errors associated with the higher mobility of the lipid-bound α -helical content, resulting in lower excitation efficiency relative to the fibril form. Additionally, the potential for a polymorph specific dependence regarding lipid-mediated restructuring may also influence the transition to helical content between the observed forms, adding to the discrepancy. This is consistent with the CD study, where the A53T and E46K polymorphs experienced slower kinetics of helical transition in comparison to the WT form. Therefore, structural differences between polymorphs of the same type (WT in this case) may play a key role in dictating both their restructuring kinetics as well as the resulting structure and dynamics in response to anionic lipid exposure.

Conserved residues assigned to the β -structure core and resolvable in the 2D spectra include N65, G84 and A85. Although most resolved peaks remained unperturbed, some extreme peak shifts can be seen in the threonine specific region and

elsewhere (**Figure 4.9 & 4.10**). Distinct peak shifts induced by lipid exposure were discoverable within both the 2D CP DARR and 2D NCA spectra involving several assigned residues: S42, T54, G68, T75, and S87-A90. Interestingly, the 2D INEPT TOBSY spectra also indicated both a perturbed C-terminal tail as well as the mobilization of several N-terminal residues (1-96), following the appearance of multiple threonine and serine correlations. Additionally, an overall reduction in the integrated intensity of β -sheet content to ~30% relative to the fibril sample was observed, suggesting overall mobilization of the fibril form upon binding to lipids.

Given that the majority of correlations indicative of the fibril core remain unperturbed, it is likely that only a small number of N-terminal residues bind to lipid membranes resulting in the observed helical structure. This partial transition of N-terminal residues to a helical conformation in the presence of lipids would be consistent with the observed anchor-like nature of the N-terminus, having a high binding affinity for anionic lipid membranes given favorable electrostatic interactions. It is presumed then that this region, which is semi-unstructured in most fibril forms, interacts with TOCL and DOPA containing LUV surfaces after exposure to form short α -helical anchors. Such binding would result in the partial transition of alanine and valine fibril content to α -helical content while largely conserving the general β -structured core, as observed. This helical stretch is likely comprised of only the first ~20 residues, as there is virtually no observable transition of threonine correlations to the helical form, consistent with the lack of threonine residues within this region, while 25% of helical alanines lie within this stretch (16 alanines between residues 1-96, with 4 located between residues 1-20).

The largest observed perturbation of the fibrils observed in this study involve residues S87-A90, normally located within the inner loops of the ‘Greek-key’ or three-layered L-shaped motif normally spanning residues ~70–90 as observed in multiple cryo-EM and ssNMR polymorphs (eg. 2N0A, 6A6B, 6CU7). However, one cryo-EM structure suggests that this inner loop containing S87-A90 is slightly open to solution, unlike most other polymorphs (eg. 6H6B).⁴⁹ Furthermore, a pathway regarding the formation of the oligomeric form via secondary nucleation suggests that the N- and C-terminus forms a “fuzzy” coat around the fibril periphery, interacting with and recruiting monomers.³⁶ It also mirrors a recently proposed membrane nucleating aggregation pathway, where monomers aggregate via NAC residues while membrane-bound by the N-terminal α -helix anchor (residues ~1-30).³² It was reported that the N- and C-terminal sides of the NAC core of fibrils and oligomers anchor to membrane surfaces, although the affinity for such binding is likely polymorph dependant.³² Specifically, residues L38-S42 were bound to lipids, with residues located in the NAC domain near the C-terminus A85-G86 and G93-V95 also showing to be in contact with lipids.³² While speculative, considering comparisons being made for aggregation and dissolution via membrane surfaces, the disappearance of S42 and perturbations of S87-A90 in the 2D CP DARR spectra for fibrils could suggest potential association of the fibril core periphery with membrane surfaces. However, such interactions cannot be verified given the current data, and other mechanisms could likely explain these changes. Further work would need to be completed in order to assess whether strands associated with the fibril core come in stable contact with the lipid membrane.

Interestingly, a recent cryo-EM study published two polymorphic structures of α -syn fibrils (polymorphs 2A and 2B, 6SSX and 6SST), one of which includes an observation potentially consistent with the results in this study.⁴⁷ They note that the hydrophobic area comprising A89, A90, A91, F94 and V95 is involved in the stabilization of an additional β -strand density, structurally illustrated in **Figure 4.12B**, a hydrophobic stretch formed by residues V16 to E20 and creating a hydrophobic steric-zipper geometry with residues S87-A91. This same region was also previously described by an NMR study done on equivalently prepared fibrils, which reported the disordered nature of residues K21 to G37, as well as correlations between S87 and A17, A18, and A19 indicating the association of these two regions.¹⁰³ Additionally, multiple MSA polymorphs studied via cryo-EM also include a structured N-terminal β -strand, indicating that there is some propensity for the N-terminus to interact with the fibril core (6XYO, 6XYP, 6XYQ) as shown in **Figure 4.12A**.⁵³ Although the fibrils utilized in this study were grown under different conditions from polymorphs 2A/2B and the complementary NMR study, these general structural features could potentially explain the perturbances experienced by residues S87-A90, given that they are consistent with the fibril form studied in this thesis. The minimum conversion to ~20% helical structure in the alanine region would suggest 3 restructured alanines, consistent with the A17-A19 stretch correlating with S87.

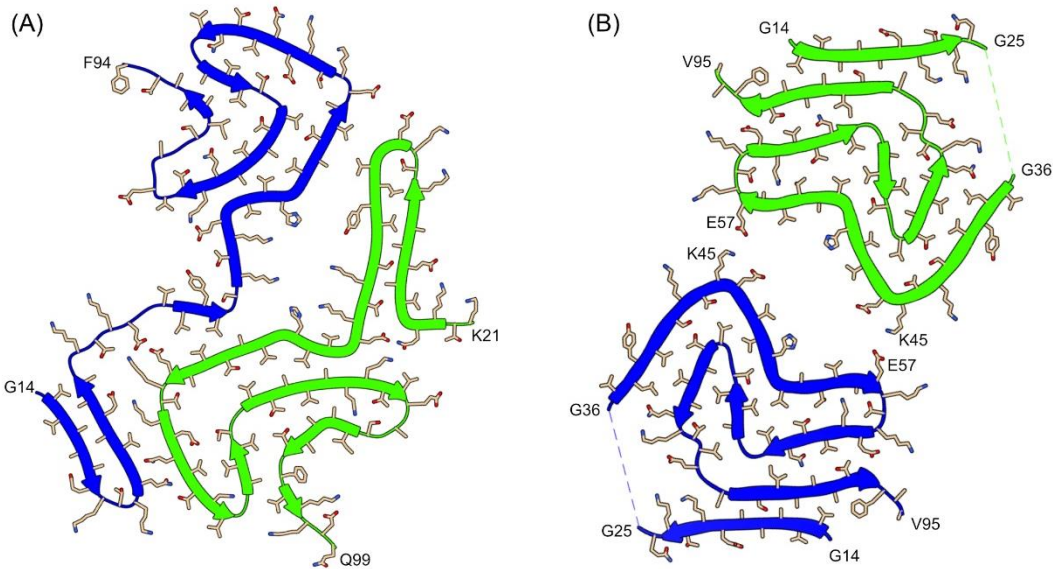


Figure 4.12: Cryo-EM cross-sections of fibril polymorphs corresponding to (A) PDB 6XYO - MSA Type I, with protofilament IA in blue and IB in green, and (B) PDB 6SSX - Polymorph 2a. Two different interprotofilament interface interactions, given steric zipper in 6XYO and **two salt-bridges** involved at the connecting interface of 6SSX (its counterpart, polymorph 6SST, contains only one). Both illustrate unique N-terminal interactions, forming a steric-zipper containing residues G14-G25 for 6SSX, and beyond for 6XYO (6SSX/6SST & 6XYO/6XYP/6XYQ).^{47,53}

The 6SSX and 6SST polymorphs containing the N-terminal wrap around, as well as the MSA polymorphs which show a similarly structured N-terminal β -strands, specifically, protofilament-b in the MSA polymorph 6XYO, are not alone in terms of N-terminal association with the core fibril structure. Another study in pre-print reports three new polymorphs obtained via PMCA (protein misfolding cyclic amplification), which like polymorph 6SSX show not just the N-terminal association, but the C-terminus bound to the fibril core as well.⁵⁷ They report rigid core association of residues 124-134, while

residues 98-123 remained unresolved. The existence of these structures is potential evidence for the association of these regions with the fibril core, providing a viable prediction of a model for the observed perturbations experienced by fibrils when exposed to anionic lipid membranes.

In summary, it appears that the fibrils utilized in this study, while distinct from those previously published based on chemical shifts and dihedral angle comparisons, may share some structural similarities. Namely, the short N-terminus region may wrap around and interact with the outside of the fibril core, consistent with the similarities between the residues involved and the resulting perturbations observed for those very same residues when exposed to anionic lipids. Assuming this structural feature (6SSX) is consistent with our fibrils, the N-terminal strand (V16 to E20) likely dissociates from the perturbed region (S87-A91) in response to electrostatic interactions with nearby anionic membranes, binding the N-terminus to lipids and resulting in the observed perturbations and increased helical structure. The release of this region from the core may also play a role in the increased mobility observed, suggesting the wrapped N-terminal strand plays a role in the stability of the fibril core. The model proposing this interaction is illustrated in **Figure 4.14**, ultimately leading to the fully dissolved monomeric form, given that such a restructuring pathway is possible.

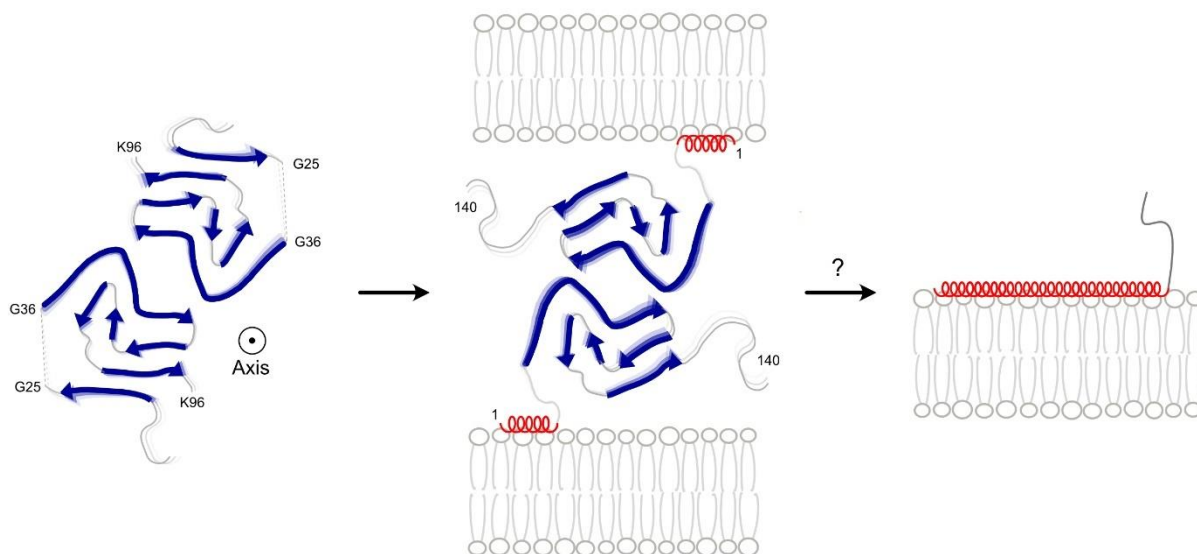


Figure 4.13: A model representation of fibril restructuring via anionic lipid interactions. Given the low PLR, the N-termini of a single fibril (illustrated here as the PDB 6SSX structure) can likely interact with multiple lipid surfaces, each binding to form partial helical structure while maintaining the general fibril core albeit with reduced rigidity given the absence of N-terminal binding to the core periphery. N-terminal binding suggests that the fibril core maintains its β -sheet secondary structure, although binding of the core to the membrane is not out of the realm of possibility. The final form is represented by the monomeric lipid-bound elongated helix, suggesting that full transition to the monomeric form is achievable, but is ultimately dependent by the fibril's polymorph structure given clear resistance to further restructuring.

By no means is this model is meant represent the exact mechanism behind the observed remodeling, and much work needs to be done in order to truly elucidate its mechanisms. However, it can be said with some confidence given our observations that although our fibril polymorph may not be susceptible to full dissolution via anionic membrane interactions, N-terminal binding likely initiates interactions with the

membranes and precludes any further restructuring for those polymorphs which are susceptible to dissolution.

5 Future Work

Ultimately, more work must be done in order to probe the fibril-lipid interactions studied in this thesis. Given the only partial assignment of the fibril core, limited conclusions could be made about the site-specific interactions taking place between fibril and anionic membranes, making the proposed model of fibril-lipid interactions only tentative. Further experiments may utilize the reported chemical shift assignments, valuable for further exploration of fibril-lipid interactions under varying scenarios, although, full assignment of the fibril core would prove useful. This would involve forming more fibrils via seeding of the original fibril form, increasing the sensitivity and resolution of the 3D NMR experiments required via sample volume alone, a project currently underway. Seeding involves adding sonicated fibrils to the α -syn stock solution prior to agitation and fibril formation, causing template-directed fibril growth via the 'seed' structure. More specifically, plans for probing lower PLR, more complex lipid compositions, and other polymorphic fibril forms will form the basis for future in-vitro studies of fibril-lipid interactions. Potential forms include a distinct low pH form and newly found fibril polymorph formed under similar conditions to those studied in this thesis, with its distinct and homologous structure more easily characterizable using NMR methods. In addition, NMR based lipid studies including ^{31}P and ^1H NMR may also elucidate important information regarding their interactions with α -syn fibrils, aiding in the potential validation of our model for fibril-lipid interactions.

Importantly, this study was performed exclusively on in vitro samples with LUVs that only mimic the OMM after externalization of CL. Therefore, conducting in-cell NMR experiments could provide a more comprehensive view of α -syn in a native environment, with the uptake of fibrils by neuroblastoma cells to directly probe native interactions with mitochondria. It is possible to isolate mitochondria from neuroblastoma cells and expose them to fibrils, forming a characterizable control sample useful in differentiating between signals of several conformers likely to be co-existing in-cell, allowing for site-specific tracking of the multiple co-existing forms of α -synuclein within cells and on mitochondrial and other cellular surfaces.

Work has been done to optimize Dynamic Nuclear Polarization (DNP) NMR for use in-cell. It is a novel method performed at cryogenic temperatures of $\sim 100\text{K}$ allowing for signal enhancements of 1-2 orders of magnitude via biologically inert paramagnetic biradicals within the sample. The paramagnetic electrons are strongly polarized via microwave radiation and polarization is subsequently transferred to nuclear spins before conducting familiar NMR experiments. This increase in sensitivity is necessary for use in exploration of in-cell samples given volume limitations (glycerol is used as a cryoprotectant, making up a large percentage of the sample volume) and limited fibril uptake by cells (on the order of several hundred micrograms, in comparison to the several milligrams found in regular NMR experiments). Methods for DNP sample preparation have been adapted from Frederick et al.¹²¹, with glycerol and AMUPol concentrations being optimized for maximum signal-to-noise enhancements.

Selective labelling schemes have also been proposed in order to reduce the spectral crowding and overlap by ensuring only specific residue pairs are visible to NMR methods.¹²² This would prove useful for both in-vitro and in-cell experiments by resolving otherwise unresolved residues. Given knowledge of metabolic pathways in *E.coli*, along with strong conformational changes between residues ~38-96 observed in our heteronuclear SSNMR experiments, five unique pairs were identified as useful structural reporters. The addition of only ¹⁵N-Ala and ¹³C-Ile during expression results in the unique pair Ile88-Ala89, located within the NAC domain. ¹⁵N-Asn and ¹³C-Thr result in the unique pair Thr64-Asn65, located at the beginning of the NAC domain. ¹⁵N-Tyr and ¹³C-Leu result in the unique pair Leu38-Tyr39, located at the beginning of the β -sheet fibril structure. His50 is the only histidine residue within the protein located at the end of the metabolic chain, making it another unique structural reporter. Finally, Thr75-Ala76 pair is accessible by addition of ¹⁵N-Ala and ¹³C-Thr but could potentially create secondary labelling given the scrambling of ¹³C from threonine to isoleucine and slight scrambling of ¹⁵N from alanine to valine. Given the suggested effects on the N-terminus of fibrils in the presence of anionic membranes in this thesis, a special pairing within this region (residues 1-20) may prove useful in probing the initial lipid-binding effect suggested by the model in **Figure 4.13**, although pairing here would give rise to scrambling effects. Using such methods and conducting more research on fibril-lipid interactions under NMR will undoubtedly uncover the mechanisms behind fibril restructuring both in vitro and in-cell, while also aiming to better understand polymorph-specific effects.

REFERENCES

- (1) Barrett, P. J.; Timothy Greenamyre, J. Post-Translational Modification of α -Synuclein in Parkinson's Disease. *Brain Res.* **2015**, *1628*, 247–253..
- (2) Osterhaus, A.; Groen, J.; Bildt, M. Van De; Martina, B.; Vos, J.; Egmond, H. Van. A -Synuclein in Lewy Bodies. *Nature* **1997**, *388*, 839–840.
- (3) Dauer, W.; Przedborski, S. Parkinson's Disease: Mechanisms and Models. *Neuron* **2003**, *39* (6), 889–909.
- (4) Thomas, B.; Flint Beal, M. Parkinson's Disease. *Hum. Mol. Genet.* **2007**, *16* (R2), 183–194.
- (5) Alderson, T. R.; Markley, J. L. Biophysical Characterization of α -Synuclein and Its Controversial Structure. *Intrinsically Disord. Proteins* **2013**, *1* (1), e26255.
- (6) Shahmoradian, S. H.; Lewis, A. J.; Genoud, C.; Hench, J.; Moors, T. E.; Navarro, P. P.; Castaño-Díez, D.; Schweighauser, G.; Graff-Meyer, A.; Goldie, K. N.; Sütterlin, R.; Huisman, E.; Ingrassia, A.; Gier, Y. de; Rozemuller, A. J. M.; Wang, J.; Paepe, A. De; Erny, J.; Staempfli, A.; Hoernschemeyer, J.; Großerüschkamp, F.; Niedieker, D.; El-Mashtoly, S. F.; Quadri, M.; Van IJcken, W. F. J.; Bonifati, V.; Gerwert, K.; Bohrmann, B.; Frank, S.; Britschgi, M.; Stahlberg, H.; Van de Berg, W. D. J.; Lauer, M. E. Lewy Pathology in Parkinson's Disease Consists of Crowded Organelles and Lipid Membranes. *Nat. Neurosci.* **2019**, *22* (7), 1099–1109.
- (7) Emamzadeh, F. N. Alpha-Synuclein Structure, Functions, and Interactions. *J. Res. Med. Sci.* **2016**, *21* (2).
- (8) Burre, J.; Sharma, M.; Tsetsenis, T.; Buchman, V.; Etherton, M. R.; Sudhof, T. C. Alpha-Synuclein Promotes SNARE-Complex Assembly in Vivo and in Vitro. *Science (80-)*. **2010**, *329* (5999), 1663–1667.
- (9) Chandra, S.; Gallardo, G.; Fernandez-Chacon, R.; Schluter, O. M.; Sudhof, T. C. Alpha-Synuclein Cooperates with CSPalpha in Preventing Neurodegeneration. *Cell* **2005**, *123* (3), 383–396.
- (10) Murphy, D. D.; Rueter, S. M.; Trojanowski, J. Q.; Lee, V. M. Synucleins Are Developmentally Expressed, and Alpha-Synuclein Regulates the Size of the Presynaptic Vesicular Pool in Primary Hippocampal Neurons. *J Neurosci* **2000**, *20* (9), 3214–3220.
- (11) Abeliovich, A.; Schmitz, Y.; Farinas, I.; Choi-Lundberg, D.; Ho, W. H.; Castillo, P. E.; Shinsky, N.; Verdugo, J. M.; Armanini, M.; Ryan, A.; Hynes, M.; Phillips, H.; Sulzer, D.; Rosenthal, A. Mice Lacking Alpha-Synuclein Display Functional

- Deficits in the Nigrostriatal Dopamine System. *Neuron* **2000**, 25 (1), 239–252.
- (12) Watson, J. B.; Hatami, A.; David, H.; Masliah, E.; Roberts, K.; Evans, C. E.; Levine, M. S. Alterations in Corticostriatal Synaptic Plasticity in Mice Overexpressing Human Alpha-Synuclein. *Neuroscience* **2009**, 159 (2), 501–513.
- (13) Lashuel, H. A.; Overk, C. R.; Oueslati, A.; Masliah, E. The Many Faces of α -Synuclein: From Structure and Toxicity to Therapeutic Target.
- (14) Fusco, G.; De Simone, A.; Arosio, P.; Vendruscolo, M.; Veglia, G.; Dobson, C. M. Structural Ensembles of Membrane-Bound α -Synuclein Reveal the Molecular Determinants of Synaptic Vesicle Affinity. *Sci. Rep.* **2016**, 6 (June).
- (15) Nuytemans, K.; Theuns, J.; Cruts, M.; Van Broeckhoven, C. Genetic Etiology of Parkinson Disease Associated with Mutations in the SNCA, PARK2, PINK1, PARK7, and LRRK2 Genes: A Mutation Update. *Hum. Mutat.* **2010**, 31 (7), 763–780..
- (16) Mor, D. E.; Ugras, S. E.; Daniels, M. J.; Ischiropoulos, H. Dynamic Structural Flexibility of α -Synuclein. *Neurobiol. Dis.* **2016**, 88, 66–74.
- (17) Comellas, G.; Lemkau, L. R.; Zhou, D. H.; George, J. M.; Rienstra, C. M. Structural Intermediates during α -Synuclein Fibrillogenesis on Phospholipid Vesicles. **2012**.
- (18) Parihar, M. S.; Parihar, A.; Fujita, M.; Hashimoto, M.; Ghafourifar, P. Mitochondrial Association of Alpha-Synuclein Causes Oxidative Stress. *Cell. Mol. Life Sci.* **2008**, 65 (7–8), 1272–1284.
- (19) Ryan, T.; Bamm, V. V.; Stykel, M. G.; Coackley, C. L.; Humphries, K. M.; Jamieson-Williams, R.; Ambasudhan, R.; Mosser, D. D.; Lipton, S. A.; Harauz, G.; Ryan, S. D. Cardiolipin Exposure on the Outer Mitochondrial Membrane Modulates α -Synuclein. *Nat. Commun.* **2018**, 9 (1), 1–17.
- (20) Chu, C. T.; Ji, J.; Dagda, R. K.; Jiang, J. F.; Tyurina, Y. Y.; Kapralov, A. A.; Tyurin, V. A.; Yanamala, N.; Shrivastava, I. H.; Mohammadyani, D.; Zhi, K.; Wang, Q.; Zhu, J.; Klein, J.; Balasubramanian, K.; Amoscato, A. A.; Huang, Z.; Gusdon, A. M.; Cheikhi, A.; Steer, E. K.; Baty, C.; Watkins, S.; Bahar, I.; Bayir, H.; Valerian, E. Cardiolipin Externalization to the Outer Mitochondrial Membrane Acts as an Elimination Signal for Mitophagy in Neuronal Cells. **2014**, 15 (10), 1197–1205.
- (21) Bartels, T.; Choi, J. G.; Selkoe, D. J. α -Synuclein Occurs Physiologically as a Helically Folded Tetramer That Resists Aggregation. *Nature* **2011**, No. 477, 107–110.

- (22) Fusco, G.; De Simone, A.; Gopinath, T.; Vostrikov, V.; Vendruscolo, M.; Dobson, C. M.; Veglia, G. Direct Observation of the Three Regions in α -Synuclein That Determine Its Membrane-Bound Behaviour. *Nat. Commun.* **2014**, *5* (May), 1–8.
- (23) Ulmer, T. S.; Bax, A.; Cole, N. B.; Nussbaum, R. L. Structure and Dynamics of Micelle-Bound Human Alpha-Synuclein. *J Biol Chem* **2005**, *280* (10), 9595–9603.
- (24) Tuttle, M. D.; Comellas, G.; Nieuwkoop, A. J.; Covell, D. J.; Berthold, D. A.; Klopper, K. D.; Courtney, J. M.; Kim, J. K.; Barclay, A. M.; Kendall, A.; Wan, W.; Stubbs, G.; Schwieters, C. D.; Lee, V. M.; George, J. M.; Rienstra, C. M. Solid-State NMR Structure of a Pathogenic Fibril of Full-Length Human Alpha-Synuclein. *Nat Struct Mol Biol* **2016**, *23* (5), 409–415.
- (25) Bodner, C. R.; Dobson, C. M.; Bax, A. Multiple Tight Phospholipid-Binding Modes of α -Synuclein Revealed by Solution NMR Spectroscopy. *J. Mol. Biol.* **2009**, *390* (4), 775–790.
- (26) Jao, C. C.; Hegde, B. G.; Chenb, J.; Haworth, I. S.; Langen, R. Structure of Membrane-Bound α -Synuclein from Site-Directed Spin Labeling and Computational Refinement. *Proc. Natl. Acad. Sci. U. S. A.* **2008**, *105* (50), 19666–19671.
- (27) Ulmer, T. S.; Bax, A.; Cole, N. B.; Nussbaum, R. L. Structure and Dynamics of Micelle-Bound Human α -Synuclein. *J. Biol. Chem.* **2005**, *280* (10), 9595–9603.
- (28) Drescher, M.; Veldhuis, G.; Van Rooijen, B. D.; Milikisyants, S.; Subramaniam, V.; Huber, M. Antiparallel Arrangement of the Helices of Vesicle-Bound α -Synuclein. *J. Am. Chem. Soc.* **2008**, *130* (25), 7796–7797.
- (29) Vallurupalli, P.; Bouvignies, G.; Kay, L. E. Studying “Invisible” Excited Protein States in Slow Exchange with a Major State Conformation. *J. Am. Chem. Soc.* **2012**, *134* (19), 8148–8161.
- (30) Fusco, G.; De Simone, A.; Gopinath, T.; Vostrikov, V.; Vendruscolo, M.; Dobson, C. M.; Veglia, G. Direct Observation of the Three Regions in α -Synuclein That Determine Its Membrane-Bound Behaviour. *Nat. Commun.* **2014**, *5* (1), 3827.
- (31) Zhu, M.; Li, J.; Fink, A. L. The Association of α -Synuclein with Membranes Affects Bilayer Structure, Stability, and Fibril Formation. *J. Biol. Chem.* **2003**, *278* (41), 40186–40197.
- (32) Antonschmidt, L.; Dervişoğlu, R.; Sant, V.; Tekwani Movellan, K.; Mey, I.; Riedel, D.; Steinem, C.; Becker, S.; Andreas, L. B.; Griesinger, C. Insights into the Molecular Mechanism of Amyloid Filament Formation: Segmental Folding of α -Synuclein on Lipid Membranes. *Sci. Adv.* **2021**, *7* (20), eabg2174.

- (33) Lee, H.-J.; Choi, C.; Lee, S.-J. Membrane-Bound Alpha-Synuclein Has a High Aggregation Propensity and the Ability to Seed the Aggregation of the Cytosolic Form. *J. Biol. Chem.* **2002**, *277* (1), 671–678.
- (34) Zhu, M.; Fink, A. L. Lipid Binding Inhibits α -Synuclein Fibril Formation. *J. Biol. Chem.* **2003**, *278* (19), 16873–16877.
- (35) Galvagnion, C.; Buell, A. K.; Meisl, G.; Michaels, T. C. T.; Vendruscolo, M.; Knowles, T. P. J.; Dobson, C. M. Lipid Vesicles Trigger α -Synuclein Aggregation by Stimulating Primary Nucleation. *Nat. Chem. Biol.* **2015**, *11* (february), 229–234.
- (36) Yang, X.; Wang, B.; Hoop, C. L.; Williams, J. K.; Baum, J. NMR Unveils an N-Terminal Interaction Interface on Acetylated- α -Synuclein Monomers for Recruitment to Fibrils. *Proceedings of the National Academy of Sciences of the United States of America*. 2021.
- (37) Tran, H. T.; Chung, C. H. Y.; Iba, M.; Zhang, B.; Trojanowski, J. Q.; Luk, K. C.; Lee, V. M. Y. α -Synuclein Immunotherapy Blocks Uptake and Templated Propagation of Misfolded α -Synuclein and Neurodegeneration. *Cell Reports*. 2014, pp 2054–2065.
- (38) Hoyer, W.; Antony, T.; Cherny, D.; Heim, G.; Jovin, T. M.; Subramaniam, V. Dependence of α -Synuclein Aggregate Morphology on Solution Conditions. *Journal of Molecular Biology*. 2002, pp 383–393.
- (39) Heise, H.; Hoyer, W.; Becker, S.; Andronesi, O. C.; Riedel, D.; Baldus, M. Molecular-Level Secondary Structure, Polymorphism, and Dynamics of Full-Length α -Synuclein Fibrils Studied by Solid-State NMR. *Proc. Natl. Acad. Sci. U. S. A.* **2005**, *102* (44), 15871–15876.
- (40) Gath, J.; Habenstein, B.; Bousset, L.; Melki, R.; Meier, B. H.; Böckmann, A. Solid-State NMR Sequential Assignments of α -Synuclein. *Biomol. NMR Assign.* **2012**, *6* (1), 51–55.
- (41) Tuttle, M. D.; Comellas, G.; Nieuwkoop, A. J.; Covell, D. J.; Berthold, D. A.; Kloepper, K. D.; Courtney, J. M.; Kim, J. K.; Barclay, A. M.; Kendall, A.; Wan, W.; Stubbs, G.; Schwieters, C. D.; Lee, V. M. Y.; George, J. M.; Rienstra, C. M. Solid-State NMR Structure of a Pathogenic Fibril of Full-Length Human α -Synuclein. *Nat. Struct. Mol. Biol.* **2016**, *23* (5), 409–415.
- (42) Wager, M. G. T. and J. F. S. Structured Regions of α -Synuclein Fibrils Include the Early-Onset Parkinson's Disease Mutation Sites. *Bone* **2011**, *23* (1), 1–7.
- (43) Zhou, D. H.; Nieuwkoop, A. J.; Berthold, D. A.; Comellas, G.; Sperling, L. J.; Tang, M.; Shah, G. J.; Brea, E. J.; Lemkau, L. R.; Rienstra, C. M. Solid-State

- NMR Analysis of Membrane Proteins and Protein Aggregates by Proton Detected Spectroscopy. *J. Biomol. NMR* **2012**, *54* (3), 291–305.
- (44) Barclay, A. M.; Dhavale, D. D.; Courtney, J. M.; Kotzbauer, P. T.; Rienstra, C. M. Resonance Assignments of an α -Synuclein Fibril Prepared in Tris Buffer at Moderate Ionic Strength. *Biomolecular NMR Assignments*. 2018, pp 195–199.
- (45) Verasdonck, J.; Bousset, L.; Gath, J.; Melki, R.; Böckmann, A.; Meier, B. H. Further Exploration of the Conformational Space of α -Synuclein Fibrils: Solid-State NMR Assignment of a High-PH Polymorph. *Biomolecular NMR Assignments*. 2016, pp 5–12.
- (46) Guerrero-Ferreira, R.; Kovacic, L.; Ni, D.; Stahlberg, H. New Insights on the Structure of Alpha-Synuclein Fibrils Using Cryo-Electron Microscopy. *Curr. Opin. Neurobiol.* **2020**, *61*, 89–95.
- (47) Guerrero-Ferreira, R.; Taylor, N. M. I.; Arteni, A. A.; Kumari, P.; Mona, D.; Ringler, P.; Britschgi, M.; Lauer, M. E.; Makky, A.; Verasdock, J.; Riek, R.; Melki, R.; Meier, B. H.; Böckmann, A.; Bousset, L.; Stahlberg, H. Two New Polymorphic Structures of Human Full-Length Alpha-Synuclein Fibrils Solved by Cryo-Electron Microscopy. *Elife* **2019**, *8*, 1–24.
- (48) Hwang, S.; Fricke, P.; Zinke, M.; Giller, K.; Wall, J. S.; Riedel, D.; Becker, S.; Lange, A. Comparison of the 3D Structures of Mouse and Human α -Synuclein Fibrils by Solid-State NMR and STEM. *Journal of Structural Biology*. 2019, pp 43–48.
- (49) Guerrero-Ferreira, R.; Taylor, N. M. I.; Mona, D.; Ringler, P.; Lauer, M. E.; Riek, R.; Britschgi, M.; Stahlberg, H. Cryo-EM Structure of Alpha-Synuclein Fibrils. *Elife* **2018**, *7* (i), 1–18.
- (50) Li, Y.; Zhao, C.; Luo, F.; Liu, Z.; Gui, X.; Luo, Z.; Zhang, X.; Li, D.; Liu, C.; Li, X. Amyloid Fibril Structure of α -Synuclein Determined by Cryo-Electron Microscopy. *Cell Research*. 2018, pp 897–903.
- (51) Li, B.; Ge, P.; Murray, K. A.; Sheth, P.; Zhang, M.; Nair, G.; Sawaya, M. R.; Shin, W. S.; Boyer, D. R.; Ye, S.; Eisenberg, D. S.; Zhou, Z. H.; Jiang, L. Cryo-EM of Full-Length α -Synuclein Reveals Fibril Polymorphs with a Common Structural Kernel. *Nature Communications*. 2018.
- (52) Strohäker, T.; Lee, S.-J.; Zweckstetter, M. Structural Heterogeneity of α -Synuclein Fibrils Amplified from Patient Brain Extracts. *Nat Commun* **2019**.
- (53) Schweighauser, M.; Shi, Y.; Tarutani, A.; Kametani, F.; Murzin, A. G.; Ghetti, B.; Matsurbara, T.; Tomita, T.; Ando, T.; Hasegawa, K.; Murayama, S.; Yoshida, M.; Hasegawa, M.; Scheres, S. H.; Goedert, M. Structures of α -Synuclein Filaments

from Multiple System Atrophy. *Nature* **2020**.

- (54) Ni, X.; McGlinchey, R. P.; Jiang, J.; Lee, J. C. Structural Insights into α -Synuclein Fibril Polymorphism: Effects of Parkinson's Disease-Related C-Terminal Truncations. *J. Mol. Biol.* **2019**, *431* (19), 3913–3919.
- (55) Gath, J.; Bousset, L.; Habenstein, B.; Melki, R.; Meier, B. H.; Böckmann, A. Yet Another Polymorph of Alpha Synuclein: Solid-State Sequential Assignments. *Biomol NMR Assign* **2014**.
- (56) Saborio, G. P.; Permanne, B.; Soto, C. Sensitive Detection of Pathological Prion Protein by Cyclic Amplification of Protein Misfolding. *Nature* **2001**, *411* (6839), 810–813.
- (57) Burger, D.; Fenyi, A.; Bousset, L.; Stahlberg, H.; Melki, R. Cryo-EM Structure of Alpha-Synuclein Fibrils Amplified by PMCA from PD and MSA Patient Brains. *bioRxiv* **2021**, 2021.07.08.451588.
- (58) Shi, L.; Ladizhansky, V. Magic Angle Spinning Solid-State NMR Experiments for Structural Characterization of Proteins; Humana Press, Totowa, NJ, 2012; pp 153–165.
- (59) Kitamura, S.; Sturtevant, J. M.; Matsumura, M.; Matthews, B. W.; Nicholson, H.; Bechtel, W. J.; Privalov, P. L.; Remington, S. J.; Anderson, W. F.; Owen, J.; Ten Eyck, L. F.; Grainger, C. T.; Suzuki, Y.; Wishart, D. S.; Sykes, B. D.; Richards, F. M. *The Chemical Shift Index: A Fast and Simple Method for the Assignment of Protein Secondary Structure through NMR Spectroscopy*; Previous Studies by Wishart et Al; 1992; Vol. 31.
- (60) Slichter, C. P. *Principles of Magnetic Resonance*, 3rd ed.; Springer-Verlag, 1990.
- (61) Cavanagh, J.; Fairbrother, W. J.; Palmer, A. G. I.; Skelton, N. J. *Protein NMR Spectroscopy*; Academic Press, 1994.
- (62) Schmidt-Rohr, K.; Spiess, H. W. *Multidimensional Solid-State NMR and Polymers*; Academic Press, 1994.
- (63) Levitt, M. H. *Spin Dynamics*; John Wiley and Sons Inc., 2001.
- (64) Maricq, M. M.; Waugh, J. S. NMR in Rotating Solids. *J. Chem. Phys.* **1979**, *70* (7), 3300–3316. <https://doi.org/10.1063/1.437915>.
- (65) Veshtort, M.; Griffin, R. G. SPINEVOLUTION: A Powerful Tool for the Simulation of Solid and Liquid State NMR Experiments. *J. Magn. Reson.* **2006**, *178* (2), 248–282.

- (66) Morcombe, C. R.; Zilm, K. W. Chemical Shift Referencing in MAS Solid State NMR. *J. Magn. Reson.* **2003**, *162* (2), 479–486.
- (67) Markley, J. L.; Bax, A.; Arata, Y.; Hilbers, C. W.; Kaptein, R.; Sykes, B. D.; Wright, P. E.; Wüthrich, K. Recommendations for the Presentation of NMR Structures of Proteins and Nucleic Acids. *Journal of Molecular Biology.* 1998, pp 933–952.
- (68) Wishart, D. S.; Bigam, C. G.; Yao, J.; Abildgaard, F.; Dyson, H. J.; Oldfield, E.; Markley, J. L.; Sykes, B. D. ¹H, ¹³C and ¹⁵N Chemical Shift Referencing in Biomolecular NMR. *Journal of Biomolecular NMR.* 1995, pp 135–140.
- (69) Herzfeld, J.; Roufosse, A.; Haberkorn, R. A.; Griffin, R. G.; Glimcher, M. J. Magic Angle Sample Spinning in Inhomogeneously Broadened Biological Systems. **1980**, *289* (1037), 459–469.
- (70) Andrew, E. R.; Bradbury, A.; Eades, R. G. Nuclear Magnetic Resonance Spectra from a Crystal Rotated at High Speed. *Nature.* 1958, p 1659.
- (71) Lowe, I. J. Free Induction Decays of Rotating Solids. *Phys. Rev. Lett.* **1959**, *2* (7), 285–287.
- (72) A. E. Bennett, R. G. Griffin, S. V. *Recoupling of Homo- and Heteronuclear Dipolar Interactions in Rotating Solids*; 1994.
- (73) Pines, A.; Gibby, M. G.; Waugh, J. S. Proton-Enhanced Nmr of Dilute Spins in Solids. *J. Chem. Phys.* **1972**, *56* (4), 1776–1777. h
- (74) Takegoshi, K.; Nakamura, S.; Terao, T. ¹³C-¹H Dipolar-Driven ¹³C-¹³C Recoupling without ¹³C Rf Irradiation in Nuclear Magnetic Resonance of Rotating Solids. *J. Chem. Phys.* **2003**, *118* (5), 2325–2341.
- (75) Morris, G. A.; Freeman, R. Enhancement of Nuclear Magnetic Resonance Signals by Polarization Transfer. *J. Am. Chem. Soc.* **1979**, *101* (3), 760–762.
- (76) Hardy, E. H.; Verel, R.; Meier, B. H. Fast MAS Total Through-Bond Correlation Spectroscopy. *J. Magn. Reson.* **2001**, *148* (2), 459–464.
- (77) Ulrich, E. L.; Akutsu, H.; Doreleijers, J. F.; Harano, Y.; Ioannidis, Y. E.; Lin, J.; Livny, M.; Mading, S.; Maziuk, D.; Miller, Z.; Nakatani, E.; Schulte, C. F.; Tolmie, D. E.; Kent Wenger, R.; Yao, H.; Markley, J. L. BioMagResBank. *Nucleic Acids Res.* **2008**, *36* (SUPPL. 1), 402–408.
- (78) Wang, Y. Probability-Based Protein Secondary Structure Identification Using Combined NMR Chemical-Shift Data. *Protein Sci.* **2002**, *11* (4), 852–861.
- (79) Medeiros, J.; Bamm, V. V.; Jany, C.; Coackley, C.; Ward, M. E.; Harauz, G.;

- Ryan, S. D.; Ladizhansky, V. Partial Magic Angle Spinning NMR ^1H , ^{13}C , ^{15}N Resonance Assignments of the Flexible Regions of a Monomeric Alpha-Synuclein: Conformation of C-Terminus in the Lipid-Bound and Amyloid Fibril States. *Biomol. NMR Assign.* **2021**, No. C1.
- (80) Cullis, P. R. *Vesicles of Variable Sizes Produced by a Rapid Extrusion Procedure*; 1986; Vol. 858.
- (81) Ryan, T.; Bamm, V. V.; Stykel, M. G.; Coackley, C. L.; Humphries, K. M.; Jamieson-Williams, R.; Ambasadhan, R.; Mosser, D. D.; Lipton, S. A.; Harauz, G.; Ryan, S. D. Cardiolipin Exposure on the Outer Mitochondrial Membrane Modulates α -Synuclein. *Nat Commun* **2018**, 9 (1), 817.
- (82) Delaglio, F.; Grzesiek, S.; Vuister, G. W.; Zhu, G.; Pfeifer, J.; Bax, A. Nmrpipe - a Multidimensional Spectral Processing System Based on Unix Pipes. *J Biomol NMR* **1995**, 6 (3), 277–293.
- (83) Keller, R. *The Computer Aided Resonance Assignment Tutorial*, first.; CANTINA Verlag : Goldau , 2004.
- (84) Grzesiek, S.; Bax, A. Improved 3D Triple-Resonance NMR Techniques Applied to a 31 KDa Protein. *J. Magn. Reson.* **1992**, 96 (2), 432–440.
- (85) Grzesiek, S.; Bax, A. Correlating Backbone Amide and Side Chain Resonances in Larger Proteins by Multiple Relayed Triple Resonance NMR. *J. Am. Chem. Soc.* **1992**, 114 (16), 6291–6293.
- (86) Zhou, D. H.; Rienstra, C. M. High-Performance Solvent Suppression for Proton Detected Solid-State NMR. *J. Magn. Reson.* **2008**, 192 (1), 167–172.
- (87) Shaka, A. J.; Keeler, J.; Frenkiel, T.; Freeman, R. An Improved Sequence for Broadband Decoupling: WALTZ-16. *J. Magn. Reson.* **1983**, 52 (2), 335–338.
- (88) McCoy, M. A.; Mueller, L. Selective Shaped Pulse Decoupling in NMR: Homonuclear ^{13}C Carbonyl Decoupling. *J. Am. Chem. Soc.* **1992**, 114 (6), 2108–2112.
- (89) Muhandiram, D. R.; Kay, L. E. Gradient-Enhanced Triple-Resonance Three-Dimensional NMR Experiments with Improved Sensitivity. *Journal of Magnetic Resonance, Series B.* 1994, pp 203–216.
- (90) Bennett, A. E.; Ok, J. H.; Griffin, R. G.; Vega, S. Chemical Shift Correlation Spectroscopy in Rotating Solids: Radio Frequency-Driven Dipolar Recoupling and Longitudinal Exchange. *J. Chem. Phys.* **1992**, 96 (11), 8624–8627.
- (91) Verel, R.; Ernst, M.; Meier, B. H. Adiabatic Dipolar Recoupling in Solid-State

- NMR: The DREAM Scheme. *J. Magn. Reson.* **2001**, 150 (1), 81–99.
- (92) Takegoshi, K.; Yano, T.; Takeda, K.; Terao, T. ^{13}C - ^1H Dipolar-Assisted Rotational Resonance in Magic-Angle Spinning. *J. Am. Chem. Soc.* **2001**, 123 (43), 10786–10787.
- (93) Morcombe, C. R.; Gaponenko, V.; Byrd, R. A.; Zilm, K. W. Diluting Abundant Spins by Isotope Edited Radio Frequency Field Assisted Diffusion. *J. Am. Chem. Soc.* **2004**, 126 (23), 7196–7197.
- (94) Falk, A. S.; Siemer, A. B. Dynamic Domains of Amyloid Fibrils Can Be Site-Specifically Assigned with Proton Detected 3D NMR Spectroscopy. *J. Biomol. NMR* **2016**, 66 (3), 159–162.
- (95) Higman, V. A. Solid-State MAS NMR Resonance Assignment Methods for Proteins. *Prog. Nucl. Magn. Reson. Spectrosc.* **2018**, 106–107, 37–65.
- (96) Ward, M. E.; Ritz, E.; Ahmed, M. A.; Bamm, V. V.; Harauz, G.; Brown, L. S.; Ladizhansky, V. Proton Detection for Signal Enhancement in Solid-State NMR Experiments on Mobile Species in Membrane Proteins. *J. Biomol. NMR* **2015**, 63 (4), 375–388.
- (97) Higman, V. A.; Flinders, J.; Hiller, M.; Jehle, S.; Markovic, S.; Fiedler, S.; van Rossum, B. J.; Oschkinat, H. Assigning Large Proteins in the Solid State: A MAS NMR Resonance Assignment Strategy Using Selectively and Extensively ^{13}C -Labelled Proteins. *J. Biomol. NMR* **2009**, 44 (4), 245–260.
- (98) Davidson, W. S.; Jonas, A.; Clayton, D. F.; George, J. M. Stabilization of α -Synuclein Secondary Structure upon Binding to Synthetic Membranes. *J. Biol. Chem.* **1998**, 273 (16), 9443–9449.
- (99) Eliezer, D.; Kutluay, E.; Bussell, R.; Browne, G. Conformational Properties of α -Synuclein in Its Free and Lipid-Associated States. *J. Mol. Biol.* **2001**, 307 (4), 1061–1073.
- (100) Theillet, F. X.; Binolfi, A.; Bekei, B.; Martorana, A.; Rose, H. M.; Stuiver, M.; Verzini, S.; Lorenz, D.; van Rossum, M.; Goldfarb, D.; Selenko, P. Structural Disorder of Monomeric Alpha-Synuclein Persists in Mammalian Cells. *Nature* **2016**, 530 (7588), 45–50.
- (101) Viennet, T.; Wördehoff, M. M.; Uluca, B.; Poojari, C.; Shaykhalishahi, H.; Willbold, D.; Strodel, B.; Heise, H.; Buell, A. K.; Hoyer, W.; Eitzkorn, M. Structural Insights from Lipid-Bilayer Nanodiscs Link α -Synuclein Membrane-Binding Modes to Amyloid Fibril Formation.
- (102) Heise, H.; Hoyer, W.; Becker, S.; Andronesi, O. C.; Riedel, D.; Baldus, M.

- Molecular-Level Secondary Structure, Polymorphism, and Dynamics of Full-Length Alpha-Synuclein Fibrils Studied by Solid-State NMR. *Proc Natl Acad Sci U S A* **2005**, *102* (44), 15871–15876.
- (103) Gath, J.; Bousset, L.; Habenstein, B.; Melki, R.; Böckmann, A.; Meier, B. H. Unlike Twins: An NMR Comparison of Two α -Synuclein Polymorphs Featuring Different Toxicity. *PLoS One* **2014**, *9* (3), 1–12.
- (104) Gopinath, T.; Nelson, S. E. D.; Soller, K. J.; Veglia, G. Probing the Conformationally Excited States of Membrane Proteins via ^1H -Detected MAS Solid-State NMR Spectroscopy. *J. Phys. Chem. B* **2017**, *121*, 4456–4465.
- (105) Siemer, A. B.; Arnold, A. A.; Ritter, C.; Westfeld, T.; Ernst, M.; Riek, R.; Meier, B. H. Observation of Highly Flexible Residues in Amyloid Fibrils of the HET-s Prion. *J. Am. Chem. Soc.* **2006**, *128* (40), 13224–13228.
- (106) Wang, Y.; Jardetzky, O. Probability-Based Protein Secondary Structure Identification Using Combined NMR Chemical-Shift Data. *Protein Sci* **2002**, *11* (4), 852–861.
- (107) Gath, J.; Bousset, L.; Habenstein, B.; Melki, R.; Meier, B. H.; Bockmann, A. Yet Another Polymorph of Alpha-Synuclein: Solid-State Sequential Assignments. *Biomol NMR Assign* **2014**, *8* (2), 395–404.
- (108) Comellas, G.; Lemkau, L. R.; Nieuwkoop, A. J.; Kloepper, K. D.; Lador, D. T.; Ebisu, R.; Woods, W. S.; Lipton, A. S.; George, J. M.; Rienstra, C. M. Structured Regions of α -Synuclein Fibrils Include the Early-Onset Parkinson's Disease Mutation Sites. *J. Mol. Biol.* **2011**, *411* (4), 881–895.
- (109) Guerrero-Ferreira, R.; Taylor, N. M.; Mona, D.; Ringler, P.; Lauer, M. E.; Riek, R.; Britschgi, M.; Stahlberg, H. Cryo-EM Structure of Alpha-Synuclein Fibrils. *Elife* **2018**, *7*.
- (110) Li, Y.; Zhao, C.; Luo, F.; Liu, Z.; Gui, X.; Luo, Z.; Zhang, X.; Li, D.; Liu, C.; Li, X. Amyloid Fibril Structure of α -Synuclein Determined by Cryo- Electron Microscopy. *Cell Res.* **2018**, *28*, 897–903.
- (111) Shi, L.; Ahmed, M. A. M.; Zhang, W.; Whited, G.; Brown, L. S.; Ladizhansky, V. Three-Dimensional Solid-State NMR Study of a Seven-Helical Integral Membrane Proton Pump-Structural Insights. *J. Mol. Biol.* **2009**, *386* (4), 1078–1093.
- (112) Wishart, D. S.; Sykes, B. D. The ^{13}C Chemical-Shift Index: A Simple Method for the Identification of Protein Secondary Structure Using ^{13}C Chemical-Shift Data. *J. Biomol. NMR* **1994**, *4* (2), 171–180..
- (113) Nelson, D. L.; Cox, M. M. *Lehninger Principles of Biochemistry*, 7th Ed.; W.H.

Freeman, 2017.

- (114) Der-Sarkissiant, A.; Jao, C. C.; Chen, J.; Langen, R. Structural Organization of α -Synuclein Fibrils Studied by Site-Directed Spin Labeling. *J. Biol. Chem.* **2003**, *278* (39), 37530–37535.
- (115) Tycko, R. Molecular Structure of Amyloid Fibrils: Insights from Solid-State NMR. *Q. Rev. Biophys.* **2006**, *39* (1), 1–55.
- (116) Fusco, G.; De Simone, A.; Gopinath, T.; Vostrikov, V.; Vendruscolo, M.; Dobson, C. M.; Veglia, G. Direct Observation of the Three Regions in α -Synuclein That Determine Its Membrane-Bound Behaviour. *Nat. Commun.* **2014**, *5* (May), 1–8.
- (117) Bodner, C. R.; Dobson, C. M.; Bax, A. Multiple Tight Phospholipid-Binding Modes of Alpha-Synuclein Revealed by Solution NMR Spectroscopy. *J. Mol. Biol.* **2009**, *390* (4), 775–790.
- (118) Fusco, G.; De Simone, A.; Gopinath, T.; Vostrikov, V.; Vendruscolo, M.; Dobson, C. M.; Veglia, G. Direct Observation of the Three Regions in α -Synuclein That Determine Its Membrane-Bound Behaviour. *Nat. Commun.* **2014**, *5* (1), 3827.
- (119) Bodles, A. M.; Guthrie, D. J. S.; Greer, B.; Brent Irvine, G. Identification of the Region of Non-A β Component (NAC) of Alzheimer's Disease Amyloid Responsible for Its Aggregation and Toxicity. *J. Neurochem.* **2001**, *78* (2), 384–395.
- (120) Giasson, B. I.; Murray, I. V. J.; Trojanowski, J. Q.; Lee, V. M. Y. A Hydrophobic Stretch of 12 Amino Acid Residues in the Middle of α -Synuclein Is Essential for Filament Assembly. *J. Biol. Chem.* **2001**, *276* (4), 2380–2386.
- (121) Costello, W. N.; Xiao, Y.; Frederick, K. K. DNP-Assisted NMR Investigation of Proteins at Endogenous Levels in Cellular Milieu. In *Methods in Enzymology*; Academic Press, 2019; Vol. 615, pp 373–406.
- (122) Lacabanne, D.; Meier, B. H.; Böckmann, A. Selective Labeling and Unlabeling Strategies in Protein Solid-State NMR Spectroscopy. *J. Biomol. NMR* **2018**, *71* (3), 141–150.

APPENDICES

Appendix 1: Supporting information for Chapter 4.1

This appendix has been republished:

Medeiros, J.; Bamm, V. V.; Jany, C.; Coackley, C.; Ward, M. E.; Harauz, G.; Ryan, S. D.; Ladizhansky, V. Partial Magic Angle Spinning NMR ^1H , ^{13}C , ^{15}N Resonance Assignments of the Flexible Regions of a Monomeric Alpha-Synuclein: Conformation of C-Terminus in the Lipid-Bound and Amyloid Fibril States. *Biomol. NMR Assign.* **2021**, <https://doi.org/10.1007/s12104-021-10020-z>.

Table A1.1 - ^1H , ^{13}C , ^{15}N Chemical Shifts of the flexible C-terminus of α -syn bound to DOPA:DOPC liposomes (AS:PA100). Chemical shifts shown in bold font indicate those obtained through assignment extension via the 2D ^{13}C - ^{13}C INEPT-TOBSY spectrum, as illustrated in Figure 4.3.

#	RES	H	N	C	CA	CB	CG1	CG2	CD1	CE
101	GLY			174.227	45.254					
102	LYS	8.035	120.523	176.586	56.414	32.878	24.728		29.003	41.987
103	ASN	8.425	119.286	175.236	53.218	39.056				
104	GLU	8.182	121.078	176.477	56.582	29.89				
105	GLU	8.187	121.023	176.92	56.731	29.902				
106	GLY	8.221	109.797	173.368	44.941					
107	ALA	7.927	124.619		50.409	18.189				
108	PRO			177.065	63.043	32.321				
109	GLN	8.384	120.576	175.925	55.78	30.006				
110	GLU	8.27	121.606	176.887	56.661	29.999				
111	GLY	8.274	109.788	173.905	45.275					
112	ILE	7.736	119.537	176.263	60.969	38.464	27.084	17.614	12.878	
113	LEU	8.133	125.617	177.26	55.068	42.11	26.835		23.402	
114	GLU	8.146	121.158	175.847	56.596	30.412				
115	ASP	8.083	120.218	175.618	54.15	41.072				

116	MET	7.912	121.165		53.118					
117	PRO			176.581	62.792	32.037				
118	VAL	8.022	120.027	175.53	61.902	32.904	21.093	20.391		
119	ASP	8.233	124.899		51.768	41.318				
120	PRO			176.907	63.586	32.502				
121	ASP	8.145	118.343	176.072	54.524	40.967				
122	ASN	7.815	118.553	175.422	53.362	39.232				
123	GLU	8.22	121.573	176.176	56.933	29.916				
124	ALA	8.04	123.316	177.289	52.408	19.03				
125	TYR	7.715	118.865	175.295	57.781	38.921				
126	GLU	7.881	122.729	175.391	55.592	30.579				
127	MET	8.132	122.923		53.177					
128	PRO			176.883	63.076	32.55				
129	SER	8.252	116.198	174.834	58.372	63.707				
130	GLU	8.325	122.395	176.476	56.571	29.987				
131	GLU	8.237	121.461	176.923	56.82	29.943				
132	GLY	8.169	109.41	173.934	45.139					
133	TYR	7.82	119.839	175.853	58.063	38.514				
134	GLN	8.096	121.682	175.105	55.64	30.142				
135	ASP	8.025	120.897	175.433	54.198	41.193				
136	TYR	7.771	119.973	174.94	57.546	39.042				
137	GLU	7.973	124.919		53.453	30.234	53.453			
138	PRO			176.803	62.906	32.651				
139	GLU	8.313	120.915	175.296	56.34	30.26				
140	ALA	7.725	130.397		53.742	20.21				

Table A1.2 - Assigned ^{13}C chemical shifts of the flexible C-terminus of α -syn bound to TOCL:DOPC liposomes based on the comparison of the 2D ^{13}C - ^{13}C INEPT-TOBSY correlation spectra to the assigned AS:PA100 (**Figure 4.1A**).

#	RES	CA	CB	CG1	CG2	CD1	CE
102	LYS	56.414	32.878	24.728		29.003	41.987
107	ALA	50.409	18.189				
112	ILE		38.464	27.084	17.614	12.878	
113	LEU		42.11	26.835		23.402	
118	VAL		32.904	21.093	20.391		
119	ASP	51.768	41.318				
124	ALA	52.408	19.03				
126	GLU	55.592	30.579				
129	SER	58.372	63.707				
137	GLU	53.453	30.234				
140	ALA	53.742	20.21				

Table A1.3 - Assigned ^{13}C chemical shifts of the flexible C-terminus of α -syn amyloid fibrils based on the comparison of the 2D ^{13}C - ^{13}C INEPT-TOBSY correlation spectra to the assigned AS:PA100 (**Figure 4.1B**).

#	RES	CA	CB	CG1	CG2	CD1	CE
102	LYS	56.414	32.878	24.728		29.003	41.987
107	ALA	50.409	18.189				
112	ILE		38.464	27.084	17.614	12.878	
113	LEU	55.068	42.11	26.835		23.402	
118	VAL	61.902	32.904	21.093	20.391		
124	ALA	52.408	19.03				
129	SER	58.372	63.707				
140	ALA	53.742	20.21				

Appendix 2: Supporting information for Chapter 4.2

Table A2.1 – Assigned ^{13}C and ^{15}N chemical shifts of the rigid amyloid fibril core.

#	RES	N	C	CA	CB	CG1	CG2	CD1	CE
41	GLY	119.181		47.674					
42	SER	111.793	171.119	58.457	67.458				
51	GLY		171.383	48.817					
52	VAL	122.345	172.461	59.991	35.929				
53	ALA	130.331	175.904	49.357	22.802				
54	THR	111.013	173.174	58.257	71.478				
55	VAL	119.803	175.115	61.171	36.33				
56	ALA	133.035	176.102	50.491	21.454				
68	GLY	95.714	173.28	44.788					
69	ALA	126.314	174.863	50.372	24.71				
70	VAL	120.551	173.706	60.299	36.479				
71	VAL	126.972	176.982	60.001	35.371				
73	GLY	123.486	174.659	49.822					
74	VAL	122.136	174.219	60.335	35.539				
75	THR	126.439	173.686	60.332	72.102				
76	ALA	126.367	172.759	51.503	16.789				
77	VAL	118.864		60.693	34.71				
78	ALA	126.211	176.621	49.873	25.516				
79	GLN	110.05	173.387	54.003	32.076				
80	LYS	118.432	173.826	54.588	36.458				
83	GLU	123.34	173.345	56.96					
84	GLY	105.919	169.667	43.91					
85	ALA	119.003	178.046	51.773	19.033				
86	GLY	113.796		45.082					
87	SER	122.27	172.593	56.281	65.266				
88	ILE	122.758	175.025	58.85	42.036				
89	ALA	127.992	172.707	51.539	16.011				
90	ALA	120.203	175.271	49.32	21.36				